Numerical Simulation of Cavitation Bubbles by Compressible Two-Phase Fluids *

Siegfried Müller†, Philippe Helluy‡, Josef Ballmann§

Abstract

The present work deals with the numerical investigation of collapsing cavitation bubbles in compressible fluids. Here the fluid of a two-phase vapor-liquid mixture is modeled by a single compressible medium. This is characterized by the stiffened gas law using different material parameters for the two phases.

For the discretization of the stiffened gas model the approach of Abgrall and Saurel is employed where the flow equations, here the Euler equations, for the conserved quantities are approximated by a finite volume scheme and an upwind discretization is used for the non-conservative transport equations of the pressure law coefficients. The original 1st order discretization is extended to higher order applying 2nd order ENO reconstruction to the primitive variables. The derivation of the non-conservative upwind discretization for the phase indicator, here the gas fraction, is presented for arbitrary unstructured grids.

The efficiency of the numerical scheme is significantly improved by employing local grid adaptation. For this purpose multiscale-based grid adaptation is used in combination with a multilevel time stepping strategy to avoid small time steps for coarse cells. The resulting numerical scheme is then applied to the numerical investigation of the collapse of a vapor bubble in a free flow field and near to a rigid wall.

1 Introduction

The formation of vapor bubbles in a liquid is called cavitation. The bubbles may grow or collapse. Lord Rayleigh discovered that pressure waves emitted during processes of cavitation [Ray17] may damage solids, e.g., ship propellers. However, the mechanisms causing the damage of the solid are far from being completely understood.

Cavitation is induced by a pressure drop in the liquid below vapor pressure. Such a pressure decrease may occur due to local acceleration of the liquid flow caused by geometrical constraints, e.g., if the liquid flows through a narrow

*This work has been performed with funding by the Deutsche Forschungsgemeinschaft in the DFG-CNRS-Forschergruppe FOR 563 "Micro-Macro Modelling and Simulation of Liquid-Vapor Flows".

†Institut für Geometrie und Praktische Mathematik, RWTH Aachen, 52056 Aachen, Germany, mueller@igpm.rwth-aachen.de

‡IRMA, 7 rue Rene-Descartes, 67084 Strasbourg Cedex, France, helluy@math.u-strasbg.fr

§Lehr- und Forschungsgebiet für Mechanik, RWTH Aachen, 52064 Aachen, Germany, ballmann@lufmech.rwth-aachen.de

orifice or around an obstacle. In this case, the pressure drops below vapor pressure, the liquid bursts and creates a free surface filled with gas and vapor – the bubble. Due to changes in the flow field, the pressure in the liquid may increase again causing the bubble to collapse. The collapse is accompanied by strong shock and rarefaction waves running into the bubble and the surrounding liquid. The inwards running shock wave focuses in the center of the bubble. This leads to extreme physical states in the interior. In addition, the shrinking of the bubble leads to a strong compression of the vapor. Both effects evoke an increase of pressure which bulges the bubble. Hereby, a dynamic oscillation process is initiated which finally leads to the collapse of the bubble. If the collapse takes place next to a boundary, flow and pressure fields become asymmetric and a liquid jet develops which is either directed towards or away from the boundary, depending on its compliance.

The investigation of the dynamics of cavitation bubbles is of special interest in different real world applications arising, for instance, in engineering, medical applications and biology such as (i) cavitation erosion of under water structures, see [NE61, BE66, PL98], (ii) lithotripsy and sonoporation, see [OI03, OW03], and (iii) cavitation–enhanced ablation of materials e.g. biological tissues, see [BNSV01a, BNSV01b, OW03]. In this regard, the investigation of cavitation can be helpful (i) to improve the resistibility of under water structures such as ship propellers and ship walls against strong pressure waves and (ii) to optimize medical laser or lithotripter applications with regard to collateral damage to sensitive tissue structures in the vicinity of the laser focus or to its sonoporation capabilities for drug delivery.

The processes taking place in the interior and exterior of the collapsing and oscillating bubble and the prediction of onset and extent of cavitation damage are still subject of theoretical and experimental research. However, small time and space scales as well as the complicated dynamics make any theoretical and experimental approach a challenge. Therefore, advanced numerical investigations are needed to reveal further information about the highly unsteady flow dynamics in the fluid.

Here we will focus on the modeling and numerical simulation of the collapse of a single bubble in a nonstationary, inviscid compressible two–phase flow. In case of spherical symmetry this has been studied by Westenberger [Wes87]. There the Euler equations for compressible liquids (Tait equation of state) and a homogenized bubbly fluid, respectively, have been considered. Investigations verified that the fluid state inside the bubble does not stay homogeneous during the collapse. Moreover, shock waves develop if the smallest bubble radius is almost obtained or the bubble growth just started again. These wave phenomena occur preferably in the liquid but they also can develop inside the bubble and there they interact with the phase boundary due to the small radius. Thereby, the frequently made assumption of incompressibility of the liquid and the homogeneity of the vapor are qualified as inappropriate. In order to validate the extreme states that may occur due to focusing effects in liquids as well as in vapor an explicit finite volume method for the spherical bubble collapse has been developed based on the Navier-Stokes equations using different equations of state, e.g., van der Waals and others, [HB98, Han98]. It could be verified that the modeling of the bubble inside by a perfect gas is only valid at moderate changes in volume.

For the numerical simulation of two–phase immiscible flows in compressible

fluids, it is distinguished in the literature between the Lagrangian and the Eulerian approach. In the Lagrangian framework the interface is typically tracked during the time evolution. There are mainly three types of techniques: (i) particle methods, e.g., Smooth Particle Hydrodynamics, where the movement of particles is simulated, cf. [Mon94, DGP98], (ii) front tracking methods where the underlying discretization undergoes a deformation due to the movement of the interface, cf. [Hym86, CGM$^+$86, KP91, Dic97], and (iii) marker methods, e.g., Marker and Cells [WHSD], Volume of Fluid [HN79], where the discretization is fixed. Typically difficulties arise if the interface changes topologically or becomes complicated. To overcome this difficulty techniques have been developed based on an Eulerian formulation wherby the interface is captured. To distinguish the two fluid phases in this formulation the underlying equations of motion are supplemented with an additional scalar equation approximating the position of the interface, for instance, a color function [BKZ92] or a level set function [OF01, Set96]. For incompressible two–phase fluid flow this has been applied with great success, see [SSO94, SAB$^+$99]. In case of compressible two–phase flow, difficulties arise at the phase boundary caused by pressure oscillations in the numerical simulation. In order to suppress these pressure oscillations, different approaches have been considered in the literature. Abgrall et al. proposed a quasi-conservative formulation [Abg96, SA99, AK01a]. Another approach, the ghost fluid method, has been developed by Fedkiw *et al.* [FAMO99, FAX01]. A modification of their ansatz has been introduced by Abgrall and Karni [AK01a, AK01b] based on a two-flux method. Recently, Sussman [Sus03] suggested a different strategy for computing growth and collapse of vapor bubbles where a level set method is coupled with a volume-of-fluid method. However, the liquid is assumed to be incompressible. These methods turn out to give good results in case of wave processes in flows of two immiscible compressible gases. For instance, in [ABM05, And07] the two-flux method is successfully used in combination with a level set method to investigate wave interactions with gas-gas interfaces. However, these methods in general fail for compressible liquid-gas flow. In the Eulerian approach the material interface is captured rather than tracked. Therefore the two phases undergo a numerical phase transition due to the smearing of the material interface. Since the pressure laws for liquids and gases typically are not valid in the same regime of phase space the numerical mixture of the phases leads to non-physical values in the numerical phase transition regime. This typically causes the crash of the computation. Among the aforementioned approaches, the stiffened gas approach of Saurel and Abgrall [SA99] seems to be presently the only method that is capable to deal with *compressible liquid-gas* flow.

In addition to an adequate mathematical model highly efficient numerical algorithms are required, which allow for a high resolution of the waves produced by the bubble oscillation and their interaction and provide qualitative and quantitative results on the dynamics of these waves. In recent years, a new adaptive concept for finite volume schemes has been developed based on multiscale techniques. First work in this regard has been published by Harten [Har94, Har95] where by means of a multiscale sequence the flux evaluation is performed. This results in a hybrid scheme working on a uniform grid. Recently, a fully adaptive concept for multiscale finite volume schemes has been developed and investigated [Mül02, CKMP03]. This new concept turns out to be highly efficient and reliable. By now, the new adaptive multiresolution concept has

been applied with great success to different applications, e.g., 2D/3D–steady and unsteady computations of compressible fluids about airfoils modeled by the Euler and Navier–Stokes equations, respectively, on block–structured curvilinear grid patches [BLM04], backward–facing step on 2D triangulations [CKP01] and simulation of a flame ball modeled by reaction–diffusion equations on 3D Cartesian grids [RS02, RSTB03]. These applications have been performed for compressible single-phase fluids. More recently, this concept has been extended to two-phase fluid flow of compressible gases, and applied to the investigation of non–stationary shock–bubble interactions on 2D Cartesian grids for the Euler equations [ABM05, And07].

In the present work the focus is on the numerical investigation of collapsing vapor bubbles in compressible fluids. Here the fluid of a two-phase vapor-liquid mixture is modeled by a single compressible medium. For the two phases we employ the stiffened gas law with different material parameters for the two phases, see Section 2. In Section 3 the stiffened gas model is discretized by the approach of Saurel and Abgrall [SA99] where the flow equations for the conserved quantities are approximated by a finite volume scheme and an upwind discretization is used for the non-conservative transport equations of the phase indicator (gas fraction). The efficiency of the resulting scheme is improved by applying *multiscale-based grid adaptation techniques*. Note that the discretization is presented in the *multi-dimensional* case on *arbitrary* grids where we employ a *higher order reconstruction* for the primitive variables. Due to the nonstationary behavior of the flow time integration is performed explicitly. The CFL condition of the highest resolution level is locally relaxed by employing the recent multilevel time stepping strategy, cf. [MS06, LMS05, LMMS06]. The resulting numerical scheme is then applied to the numerical investigation of the collapse of a vapor bubble, see Section 4.

2 Mathematical Model

Compressible fluid flow is characterized in continuum mechanics by the fields of density ϱ, velocity $\mathbf{v}$, internal energy e and pressure p distributions. The balances of mass, momentum and energy for inviscid flow lead to the Euler equations in conservation form

$$\begin{aligned} &\varrho_t + \operatorname{div}(\varrho \mathbf{v}) = 0, \\ &(\varrho \mathbf{v})_t + \operatorname{div}(\varrho \mathbf{v} \otimes \mathbf{v} + p\mathbf{I}) = \mathbf{0}, \\ &(\varrho E)_t + \operatorname{div}(\varrho \mathbf{v}(E + p/\varrho)) = 0, \end{aligned} \tag{1}$$

where $E = e + 0.5\,\mathbf{v}^2$ is the total energy. In order to take into account the two different fluids (a gas and a liquid) we introduce a new unknown φ that we call the fraction of gas. We make the convention that $\varphi = 0$ and $\varphi = 1$ correspond to pure liquid and vapor, respectively. Because we are interested in very high speed flows and very short observation times we suppose that the phase transition can be neglected so that there is no mass transfer between the two fluids. Thus the fraction satisfies a homogeneous transport equation, i.e., its material derivative is vanishing,

$$\varphi_t + \mathbf{v} \cdot \nabla \varphi = 0. \tag{2}$$

If at the initial time $t = 0$ the fraction φ takes only the values 1 or 0, it will remain true for $t > 0$. Thus there is no physical mixing in the continuous model. However, the numerical model will introduce artificial mixture zones where $0 < \varphi < 1$. This causes some difficulties that are discussed below. Anyway, with a good numerical approximation, the size of the mixture region will tend to zero with the size of the cells in the mesh.

Using the mass conservation law, equation (2) can be written in an equivalent conservative form

$$(\varrho\varphi)_t + \mathrm{div}(\varrho\varphi\mathbf{v}) = 0, \tag{3}$$

which expresses the mass conservation of each fluid.

In order to close the system, we have to provide a pressure law

$$p = p(\varrho, e, \varphi). \tag{4}$$

In this work, we consider a relatively simple pressure law: the stiffened gas pressure law suggested in [CS97] and [Abg96]. It reads

$$p(\varrho, e, \varphi) = (\gamma(\varphi) - 1)\varrho e - \gamma(\varphi)\pi(\varphi). \tag{5}$$

If we were only studying the continuous model, it would be sufficient to provide the values of the pressure law coefficients γ and π for $\varphi = 0$ or $\varphi = 1$. But because of the numerical mixture, it is necessary to interpolate γ and π for $0 < \varphi < 1$. An arbitrary choice of interpolation would lead to numerical difficulties that are studied in many works [Abg96], [BHR03], [GHS03], *etc.* and commented below.

It appears that a good choice consists in a linear interpolation of the two special quantities β_1 and β_2 defined by

$$\begin{cases} \beta_1 = \dfrac{1}{\gamma - 1} \\ \beta_2 = \dfrac{\gamma\pi}{\gamma - 1} \end{cases} \quad \Leftrightarrow \quad \begin{cases} \gamma = 1 + \dfrac{1}{\beta_1} \\ \pi = \dfrac{\beta_2}{1 + \beta_1} \end{cases} . \tag{6}$$

The pressure law in the numerical mixture zone is then constructed as follows. First, γ and π are deduced from measurements in the pure fluids. A possible procedure is explained in [CS97]. For water and air the material coefficients for the pure phases are listed in Table 1. This gives $\gamma(0)$, $\pi(0)$ for the pure liquid and $\gamma(1)$, $\pi(1)$ for the pure vapor. We deduce then from (6) the quantities $\beta_1(0)$, $\beta_2(0)$, $\beta_1(1)$, $\beta_2(1)$ and, by a linear interpolation

$$\begin{aligned} \beta_1(\varphi) &= \varphi\beta_1(1) + (1 - \varphi)\beta_1(0), \\ \beta_2(\varphi) &= \varphi\beta_2(1) + (1 - \varphi)\beta_2(0). \end{aligned} \tag{7}$$

The mixture pressure law coefficients $\gamma(\varphi)$ and $\pi(\varphi)$ are then obtained from the reverse relation in (6).

To the stiffened gas pressure law (5) we can associate a temperature scale T. The temperature scale is compatible with thermodynamics if it is possible to find an entropy function s such that

$$Tds = de + pd(1/\varrho). \tag{8}$$

		Vapor (Air)	Liquid (Water)
γ	[-]	1.4	7.15
π	[Pa]	0	3.e+8
c_v	[J/kg K]	717.5	201.1

Table 1: Material coefficients

Several choices are possible. The simplest corresponds to

$$c_v T = e - \frac{\pi}{\varrho}, \tag{9}$$

where the constant c_v is the specific heat at constant volume, cf. [BH05]. The temperature law has no physical meaning in the artificial mixture region because our mixture pressure law has been selected for numerical reasons and not from physical arguments. Since $\gamma = 1 + \mathcal{R}/c_v$ holds in the pure phases, interpolated values for the heat capacity c_v and the specific gas constant $\mathcal{R}$ in the mixture region are computed by

$$\begin{aligned} c_v(\varphi) &= \frac{c_v(0)\, c_v(1)(\gamma(1) - \gamma(0))}{c_v(0)(\gamma(\varphi) - \gamma(0)) + c_v(1)(\gamma(1) - \gamma(\varphi))}, \\ \mathcal{R}(\varphi) &= \frac{c_v(1)\,\mathcal{R}(0)(\gamma(1) - \gamma(\varphi)) + c_v(0)\,\mathcal{R}(1)(\gamma(\varphi) - \gamma(0))}{c_v(0)(\gamma(\varphi) - \gamma(0)) + c_v(1)(\gamma(1) - \gamma(\varphi))}. \end{aligned}$$

These interpolated values have no clear physical meaning but will be used for a numerical study of the temperature in the mixture region. They are motivated by [BH05].

Finally, we remark that instead of (2) we might equivalently solve the evolution equations for the material parameters $\boldsymbol{\beta} = (\beta_1, \beta_2)$, which have vanishing material derivatives as they depend only on φ according to eq. (7)

$$\boldsymbol{\beta}_t + \boldsymbol{v} \cdot \nabla \boldsymbol{\beta} = \mathbf{0}. \tag{10}$$

3 Numerical Discretization

The numerical discretization of compressible two-phase fluid flow is still a challenge. The naive approach to apply a standard finite volume discretization to the coupled system in conservation form (1) and (3) fails to work because of pressure oscillations at the material interface. Cures have been proposed in recent years [Kar94], [FAMO99], [Abg88], [SA99], [WK05]. They are based on non-conservative schemes and are successful for gas-gas interfaces. For liquid-gas interfaces the computations will typically crash after a few time steps. One typically observes severe pressure oscillations at the phase interface due to the numerical diffusion of the density. For the stiffened gas model as summarized in Section 2 the approach of Saurel and Abgrall [SA99] is working robustly also for liquid-gas interfaces. The basic idea is to apply a finite volume scheme to the flow equations (1) and to employ an upwind discretization of the non-conservative transport equations for the pressure law coefficients (10). Here we summarize the discretization in the *multi-dimensional* case on *arbitrary* grids

where we employ a *higher order reconstruction* for the conserved variables. The efficiency of the resulting scheme is improved by applying recent *multiscale-based grid adaptation techniques* and a *multilevel time stepping strategy*.

3.1 Finite Volume Discretization of Conserved Variables

The Euler equations (1) are solved approximately by a finite volume method. For this purpose the finite fluid domain $\Omega \subset \mathbb{R}^d$ is split into a finite set of subdomains, the cells V_i, such that all V_i are disjoint at each instant of time and that their union gives Ω. Furthermore let $\mathcal{N}(i)$ be the set of cells that have a common edge with the cell i, and for $j \in \mathcal{N}(i)$ let $\Gamma_{ij} := \partial V_i \cap \partial V_j$ be the interface between the cells i and j and $\boldsymbol{n}_{ij}$ the outer normal of Γ_{ij} corresponding to cell i. The time interval is discretized by $t^{n+1} = t^n + \Delta t$ assuming a constant time step size. On this particular discretization the finite volume scheme can be written as

$$\boldsymbol{u}_i^{n+1} = \boldsymbol{u}_i^n - \frac{\Delta t}{|V_i|} \sum_{j \in \mathcal{N}(i)} |\Gamma_{ij}| \, \boldsymbol{F}(\boldsymbol{u}_{ij}^n, \boldsymbol{u}_{ji}^n, \boldsymbol{n}_{ij}) \tag{11}$$

using an explicit time discretization to compute the approximated cell averages $\boldsymbol{u}_i^{n+1}$ of the conserved variables $\boldsymbol{u} = (\varrho, \varrho\,\boldsymbol{v}, \varrho\,E)$ on the new time level. Here the numerical flux function $\boldsymbol{F}(\boldsymbol{u}, \boldsymbol{w}, \boldsymbol{n})$ is an approximation for the flux

$$\boldsymbol{f}(\boldsymbol{u}, \boldsymbol{n}) := \begin{pmatrix} \varrho\,\boldsymbol{v} \\ \varrho\,\boldsymbol{v} \otimes \boldsymbol{v} + p\,\boldsymbol{I} \\ \varrho\,\boldsymbol{v}\,(E + p/\varrho) \end{pmatrix} \cdot \boldsymbol{n} = \begin{pmatrix} \varrho\,v_n \\ \varrho\,v_n\,\boldsymbol{v} + p\,\boldsymbol{n} \\ \varrho\,v_n\,(E + p/\varrho) \end{pmatrix} \tag{12}$$

in outer normal direction $\boldsymbol{n}_{ij}$ on the edge Γ_{ij}. Here $v_n = \boldsymbol{v}\,\boldsymbol{n}$ is the normal velocity component. The numerical flux is assumed to be *consistent*, i.e.,

$$\boldsymbol{F}(\boldsymbol{u}, \boldsymbol{u}, \boldsymbol{n}) := \boldsymbol{f}(\boldsymbol{u}, \boldsymbol{n}). \tag{13}$$

For simplicity of presentation we neglect that due to higher order reconstruction of the values $\boldsymbol{u}_{ij}^n$ and $\boldsymbol{u}_{ji}^n$ at the cell interface Γ_{ij} it usually depends on an enlarged stencil of cell averages. Furthermore, the pressure law is applied when computing the numerical flux. Therefore it also depends on the fraction vector $\boldsymbol{Y}$ or the vector of pressure law coefficients $\boldsymbol{\beta}$, respectively, associated to the states $\boldsymbol{u}_{ij}^n$ and $\boldsymbol{u}_{ji}^n$.

Since a reasonable numerical method should at least be able to maintain a constant flow field, i.e., if $\boldsymbol{u}(\boldsymbol{x}, t) = \boldsymbol{u}_\infty$ for all $(\boldsymbol{x}, t)$, we require that the numerical solution fulfills $\boldsymbol{u}_i^n = \boldsymbol{u}_\infty$ for all index pairs (i, n), too. From the consistency of the numerical fluxes (13) and the discretizations (11) we then obtain for each cell V_i the geometric consistency condition

$$\sum_{j \in N(i)} |\Gamma_{ij}| \boldsymbol{n}_{ij} = \boldsymbol{0}. \tag{14}$$

In order to fix the numerical flux we have to choose the Riemann solver and the reconstruction method. According to Saurel and Abgrall [SA99] these have to be chosen such that a moving contact discontinuity is preserved in one spatial dimension. In higher dimensions we therefore require that the condition

$$\boldsymbol{v}_i^n = \boldsymbol{v} = const,\ p_i^n = p = const \quad \Longrightarrow \quad \boldsymbol{v}_i^{n+1} = \boldsymbol{v},\ p_i^{n+1} = p \tag{15}$$

holds for all cells i in the computational domain, i.e., constant pressure and velocity fields are preserved. Note that this condition characterizes a contact discontinuity only in 1D. In higher dimensions the scheme does not necessarily preserve the normal velocity if there is a jump in the tangential component of the velocity.

For this purpose, in our computations the Riemann problem at the cell interface is solved exactly by the Riemann solver of Colella and Glaz [CG85] originally developed for real gases. Here we apply it to stiffened gases where we modify the implementation of the solver as described in [Mül93].

Furthermore, we use a higher order reconstruction which is applied componentwise to the primitive variables $(\varrho, \boldsymbol{v}, p, \boldsymbol{\beta})$. The reconstruction of conserved variables or characteristic variables violates the consistency condition (15) and will cause oscillations at the material interface.

In our computations the underlying discretization is always a hierarchy of Cartesian grids. Therefore we employ a quasi one-dimensional second-order ENO reconstruction and Taylor expansion according to [HEOC87] to improve both the spatial and temporal accuracy. See also [Mül93] for details on the implementation.

3.2 Upwind Discretization of Non-Conservative Transport Equations for Pressure Law Coefficients

By (11) the conserved quantities can be evolved time. In addition, we also have to update the fractions before we can proceed with the next time step. However discretizing the evolution equations (2) or (3), respectively, will lead to oscillations at the material interface and spoils the computation. Therefore Saurel and Abgrall in [SA99] suggested to use an upwind discretization of the non-conservative transport equations (10) for the vector of pressure law coefficients. This is motivated by the requirement that the scheme has to preserve a contact wave for which the tangential component of the velocity is continuous in the sense of (15). A detailed derivation of the discretization in 1D can be found in [Bar02]. This can be extended to the multi-dimensional case on arbitrary grids as shall be summarized in the following. For this purpose, we assume that $\boldsymbol{v}_i^n = \boldsymbol{v}$ and $p_i^n = p$ holds for all cells i. Since the reconstruction is performed on the primitive variables we obtain $p_{ij}^n = p_{ji}^n = p$ and $\boldsymbol{v}_{ij}^n = \boldsymbol{v}_{ji}^n = \boldsymbol{v}$ whereas the reconstruction of the density ϱ and the material parameters $\boldsymbol{\beta}$ may jump across the cell interface, i.e., $\varrho_{ij}^n \neq \varrho_{ji}^n$ and $\boldsymbol{\beta}_{ij}^n \neq \boldsymbol{\beta}_{ji}^n$. Then the numerical flux computed by the exact Riemann solver is determined by

$$\boldsymbol{F}(\boldsymbol{u}_{ij}^n, \boldsymbol{u}_{ji}^n, \boldsymbol{n}_{ij}) = \begin{pmatrix} \overline{\varrho}_{ij}\, \overline{v}_{n,ij} \\ \overline{\varrho}_{ij}\, \overline{v}_{n,ij}\, \boldsymbol{v} + p\, \boldsymbol{n}_{ij} \\ \overline{\varrho}_{ij}\, \overline{v}_{n,ij}\, (\overline{E}_{ij} + p/\overline{\varrho}_{ij}) \end{pmatrix} \tag{16}$$

where $\overline{\varrho}_{ij}$, $\overline{v}_{n,ij}$ and $\overline{E}_{ij}$ are the density, normal velocity and total energy computed by the Riemann solver. Since the underlying velocity field is homogeneous

$$\overline{v}_{n,ij} = \boldsymbol{v}\, \boldsymbol{n}_{ij} \tag{17}$$

holds. The material parameters jump only across the material interface, i.e.,

$$\overline{v}_{n,ij}\, \overline{\boldsymbol{\beta}}_{ij} = \boldsymbol{\beta}_{ij}^n\, \max(\overline{v}_{n,ij}, 0) + \boldsymbol{\beta}_{ji}^n\, \min(\overline{v}_{n,ij}, 0). \tag{18}$$

We now plug in (16) into (11). Then we obtain for the discrete continuity equation

$$\varrho_i^{n+1} = \varrho_i^n - \frac{\Delta\, t}{|V_i|} \sum_{j \in \mathcal{N}(i)} |\Gamma_{ij}|\, \overline{\varrho}_{ij}\, \overline{v}_{n,ij}. \tag{19}$$

The discrete momentum equation reads

$$(\varrho \boldsymbol{v})_i^{n+1} = (\varrho \boldsymbol{v})_i^n - \frac{\Delta\, t}{|V_i|} \sum_{j \in \mathcal{N}(i)} |\Gamma_{ij}|\, (\overline{\varrho}_{ij}\, \overline{v}_{n,ij}\, \boldsymbol{v} + p\, \boldsymbol{n}_{ij}). \tag{20}$$

From (19) and (14) we then conclude $(\varrho \boldsymbol{v})_i^{n+1} = \boldsymbol{v}\, \varrho_i^{n+1}$ and, hence, $\boldsymbol{v}_i^{n+1} = \boldsymbol{v}$. Finally, the discrete energy equation reads

$$(\varrho\, E)_i^{n+1} = (\varrho\, E)_i^n - \frac{\Delta\, t}{|V_i|} \sum_{j \in \mathcal{N}(i)} |\Gamma_{ij}|\, \overline{\varrho}_{ij}\, \overline{v}_{n,ij}\, (\overline{E}_{ij} + p/\overline{\varrho}_{ij}). \tag{21}$$

Since $E = e + 0.5\, \boldsymbol{v}^2$ we deduce a discrete evolution equation for the internal energy. Using (20) and (14) it is given by

$$(\varrho\, e)_i^{n+1} = (\varrho\, e)_i^n - \frac{\Delta\, t}{|V_i|} \sum_{j \in \mathcal{N}(i)} |\Gamma_{ij}|\, \overline{\varrho}_{ij}\, \overline{v}_{n,ij}\, \overline{e}_{ij}. \tag{22}$$

From the pressure law (5) and equation (22) we then conclude that $p_i^{n+1} = p_i^n = p$ holds provided that the pressure law coefficients satisfy the discrete evolution equations

$$\boldsymbol{\beta}_i^{n+1} = \boldsymbol{\beta}_i^n - \frac{\Delta\, t}{|V_i|} \sum_{j \in \mathcal{N}(i)} |\Gamma_{ij}|\, \overline{v}_{n,ij}\, \overline{\boldsymbol{\beta}}_{ij}. \tag{23}$$

These are sufficient but not necessary conditions. Note that (23) is a non-conservative upwind discretization for the evolution equations (10) of the material parameters because $\overline{v}_{n,ij}\, \overline{\boldsymbol{\beta}}_{ij} \neq -\overline{v}_{n,ji}\, \overline{\boldsymbol{\beta}}_{ji}$. Furthermore, we remark that (23) coincides with the 1D discretization in [SA99, Bar02]. To see this we rewrite the sum in (23) by means of (14) and (17), (18) as

$$\sum_{j \in \mathcal{N}(i)} |\Gamma_{ij}|\, \overline{v}_{n,ij}\, \overline{\boldsymbol{\beta}}_{ij} = \sum_{j \in \mathcal{N}(i)} |\Gamma_{ij}|\, \overline{v}_{n,ij}\, (\overline{\boldsymbol{\beta}}_{ij} - \boldsymbol{\beta}_i^n) \tag{24}$$

Finally we obtain the upwind discretization of the pressure law coefficients

$$\boldsymbol{\beta}_i^{n+1} = \boldsymbol{\beta}_i^n - \frac{\Delta\, t}{|V_i|} \sum_{j \in \mathcal{N}(i)} |\Gamma_{ij}|\, \overline{v}_{n,ij}\, (\overline{\boldsymbol{\beta}}_{ij} - \boldsymbol{\beta}_i^n) \tag{25}$$

where in general the velocity of the material interface in normal direction $\overline{v}_{n,ij}$ is not given by (17) but results from solving the Riemann problem.

Then the numerical discretization of the two-phase fluid model consists of the following steps in each time step:

1) compute the reconstruction of the primitive variables,

2) solve the Riemann problem for each cell interface,

3) evolve density, momentum and energy in time by (11) where the numerical fluxes at the cell interfaces are determined by (12) with $\boldsymbol{u}$ the solution of the Riemann problem;

4) evolve the pressure law coefficients in time by (25) where the transport velocities at each cell interface are determined by the velocities of the Riemann solution.

Since the transport scheme (23) and (25), respectively, is linear in φ and due to the linear interpolation (7) of $\boldsymbol{\beta}$, it is equivalent to solve the evolution equation for the fraction φ, i.e.,

$$\varphi_i^{n+1} = \varphi_i^n - \frac{\Delta t}{|V_i|} \sum_{j \in \mathcal{N}(i)} |\Gamma_{ij}| \, \overline{v}_{n,ij} \, \overline{\varphi}_{ij} = \varphi_i^n - \frac{\Delta t}{|V_i|} \sum_{j \in \mathcal{N}(i)} |\Gamma_{ij}| \, \overline{v}_{n,ij} \, (\overline{\varphi}_{ij} - \varphi_i^n). \tag{26}$$

3.3 Multiscale-Based Grid Adaptation

The numerical simulation of collapsing bubbles is a highly dynamical process of compression and rarefaction waves and their interaction with the material boundary and solid walls, cf. [ABM05]. In order to catch properly all these effects high resolution discretizations are needed. However, uniform discretizations are too much time- and memory-consuming. Therefore highly efficient schemes are needed that adapt the grid to the flow solution such that a high resolution is only locally accessed where strong variations in the flow field occur. In order to improve the efficiency of the numerical scheme presented in Section 3.1 and 3.2 we employ recent multiscale-based grid adaptation techniques. By many applications these have been proven to be very efficient and reliable. Here we briefly summarize the basic conceptual ideas. For technical details we refer the reader to [Mül02], [CKMP03] and[BLM04].

Step 1: Multiscale analysis. The fundamental idea is to present the cell averages $\hat{\boldsymbol{u}}_L$ representing the discretized flow field at fixed time level t^n on a given uniform highest level of resolution $l = L$ (*reference mesh*) associated with a given finite volume discretization (*reference scheme*) as cell averages on some coarsest level $l = 0$ where the fine scale information is encoded in arrays of *detail coefficients* $\boldsymbol{d}_l$, $l = 0, \ldots, L-1$ of ascending resolution, see Figure 2. For this purpose one might use Harten's discrete concept of reconstruction and prediction, cf. [ADH98], or biorthogonal wavelets, cf. [CDP96].

The multiscale decomposition is performed on a hierarchy of *nested* grids $\mathcal{G}_l$ with increasing resolution $l = 0, \ldots, L$, see Figure 1. In our computations presented here we confine to structured curvilinear grids though the general framework is not restricted to this configuration but can also be applied to *unstructured* grids and *irregular* grid refinements in arbitrary space dimensions.

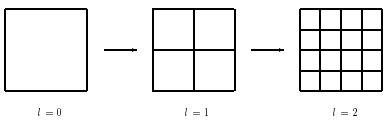

Figure 1: Sequence of nested grids

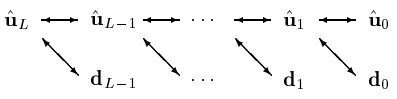

Figure 2: Multiscale transformation

Step 2: Thresholding. It can be shown that the detail coefficients become small with increasing refinement level when the underlying function is locally smooth. In order to compress the original data this motivates us to discard all detail coefficients $d_{l,\lambda}$ whose absolute values fall below a level-dependent threshold value $\varepsilon_l = 2^{l-L}\varepsilon$. Let $\mathcal{D}_{L,\varepsilon}$ be the set of *significant details*. The ideal strategy would be to determine the threshold value ϵ such that the *discretization error* of the reference scheme, i.e., difference between exact solution and reference scheme, and the *perturbation error*, i.e., the difference between the reference scheme and the adaptive scheme, are balanced, see [CKMP03].

Step 3: Prediction and grading. Since the flow field evolves in time, grid adaptation is performed after each evolution step to provide the adaptive grid at the *new* time level. In order to guarantee the adaptive scheme to be *reliable* in the sense that no significant future feature of the solution is missed, we have to *predict* all significant details at the new time level $n+1$ by means of the details at the *old* time level n. Let $\tilde{\mathcal{D}}_{L,\varepsilon}^{n+1} \supset \mathcal{D}_{L,\varepsilon}^{n} \cup \mathcal{D}_{L,\varepsilon}^{n+1}$ be the prediction set. The prediction strategy is detailed in [CKMP03]. In view of the grid adaptation step this set is additionally inflated such that it corresponds to graded tree.

Step 4: Grid adaptation. By means of the set $\tilde{\mathcal{D}}_{L,\varepsilon}^{n+1}$ a locally refined grid is determined. For this purpose, we recursively check proceeding levelwise from coarse to fine whether there exists a significant detail to a cell. If there is one, then we refine the respective cell. We finally obtain the locally refined grid with hanging nodes represented by the index set $\mathcal{G}_{L,\varepsilon}$. This procedure is graphically sketched in Figure 3. To each shaded cell there is at least one significant detail. These cells are removed and replaced by their children on the next higher level. This results in a grid with hanging nodes.

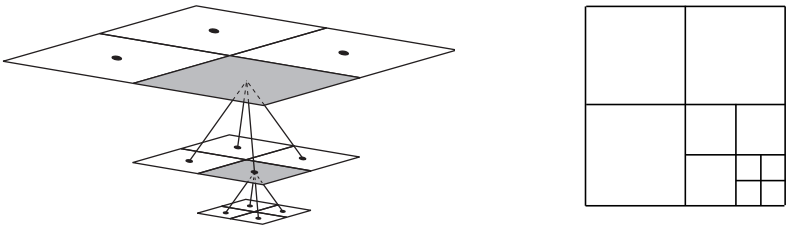

Figure 3: Grid adaptation: refinement tree (left) and corresponding adaptive grid (right)

Since the concept of multiscale-based grid adaptation has been presented and discussed in detail in previous publications we omit the technical details needed to realize it. However, we comment on some aspects that were not addressed in single-phase computations. Note, that the grid adaptation concept has been developed and investigated originally for finite volume schemes. Here the numerical discretization is a hybrid scheme where the conserved variables $\boldsymbol{u}$ of mass, momentum and energy are discretized by a finite volume scheme (11) and the pressure law coefficients $\boldsymbol{\beta}$ by an upwind discretization (25) in non-conservative form. Nevertheless, we can apply the grid adaptation to the conserved and non-conserved variables although two changes have to be made to account for the extension to two-phase fluid flow and the non-conservative dis-

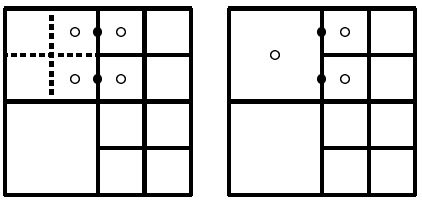

Figure 4: Flux evaluation at interface with hanging node: adaptive grid (right), virtually refined grid (left)

cretization of the pressure law coefficients. These concern the threshold process and the flux computation at hanging nodes.

Threshold process. Since the physical states in liquid and vapor differ extremely in scale it turned out in our computations that we had to modify slightly the threshold process. In previous single-phase computations, cf. [BLM04], the details for each physical quantity was scaled by its maximum in the entire computational domain. This has been useful to adjust the scales of the different quantities. Otherwise, different threshold values ε have to be used for the different quantities that usually differ by several orders of magnitude. In the present two-phase computations, this turned out to be inadequate. Due to the huge values in the liquid the maximum for each quantity is large and scaling by it would make the details corresponding to the vapor phase very small and they would be discarded in the threshold process. Hence waves in the vapor phase would not be properly resolved. Therefore we had to replace the global maximum by a local maximum where only the cells in the stencil of the detail are taken into account.

Flux computation at hanging nodes. Another issue that had to be adjusted concerns the computation of the gradients in (25) at interfaces with hanging nodes. For the numerical fluxes in (11) the strategy was unchanged. First the numerical fluxes on the higher scale are computed by values on the same refinement level. In case the neighboring cells correspond to higher or lower scales the data are projected to the respective level by means of the multi-scale transformation. Then the numerical flux on the coarser scale is the sum of all fluxes on higher scale by which the coarse interface is composed. This is shown in Figure 4. This procedure is motivated by applying the multiscale decomposition to the evolution equations (11). Then by the conservation property the fluxes corresponding to internal fluxes cancel and only the fine-grid fluxes contribute to the edges of the coarse-grid cells, see Figure 5. Similarly, we proceed with the evolution equations (25). However, due to the non-conservative discretization, the gradients at the internal interfaces do not cancel. Thus, neglecting these terms will introduce some additional error to the threshold error resulting from higher refinement levels. Nevertheless, to add the fine-grid gradients corresponding to a coarse-grid edge give satisfactory results and the *non-conservation error* does not spoil the overall accuracy of the computation.

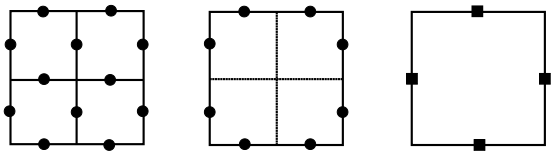

Figure 5: Flux computation: fine grid (left), cancellation due to conservation (middle), coarse grid (right)

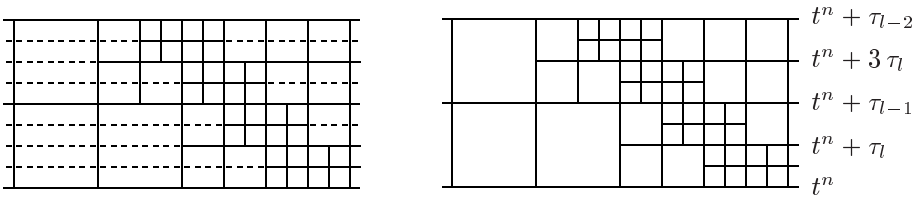

Figure 6: Synchronized time evolution on space-time grid

3.4 Multilevel Time Stepping

Since the reference scheme (11) is assumed to use an explicit time discretization, the time step size is bounded due to the CFL condition by the smallest cell in the grid. Hence Δt is determined by the highest refinement level L, i.e., $\Delta t = \tau_L$. However, for cells on the coarser scales $l = 0, \ldots, L-1$ we may use $\Delta t = \tau_l = 2^{L-l}\,\tau_L$ to satisfy locally the CFL condition. In [MS06] a multilevel time stepping strategy has been incorporated recently to the adaptive multiscale finite volume scheme as proposed in [Mül02]. It has been extended to multidimensional problems in [LMS05, LMMS06]. The basic idea is to save flux evaluations where the local CFL condition allows a large time step. The precise time evolution algorithm is schematically described by Fig. 6: In a global time stepping, i.e., using $\Delta t = \tau_L$ for all cells, each vertical line section appearing in Fig. 6 (left) represents a flux evaluation and each horizontal line (dashed or solid) represents a cell update of $\boldsymbol{u}$ due to the fluxes. In the multilevel time stepping a flux evaluation is only performed at vertical line sections that emanate from a point where at least one solid horizontal line section emanates from. If a vertical line section emanates from a point, where two dashed horizontal sections emanate from, then we do not recompute the flux, but keep the flux value from the preceeding vertical line section. Hence fluxes are only computed for the vertical edges in Fig. 6 (right).

Note, that on each intermediate time level (horizontal lines) $\boldsymbol{u}$ is updated for *all* cells and that grid adaptation is performed at each *even* intermediate time level, i.e., at $t^n + k\,\tau_L$ for k even. Hence it is possible to track, for instance, a shock movement on the intermediate time levels instead of a–priori refining the whole range of influence, see Fig. 6 (right).

However, the update of $\boldsymbol{u}$ for the conserved quantities and the material coefficients makes it necessary to modify the computation of the fluxes corresponding to a coarse cell at grid interface points, i.e., a dashed and a drawn horizontal line emanate from this point. Here the non-conservative fluxes for the material coefficients are not updated to account for the consistency condition (15)

whereas the conservative fluxes for the conserved quantities are updated by the new values on the intermediate time level.

4 Numerical Results

We are interested in the numerical investigation of the collapse of a vapor bubble far away from and next to a rigid wall, see Figure 7. These are modeled by the

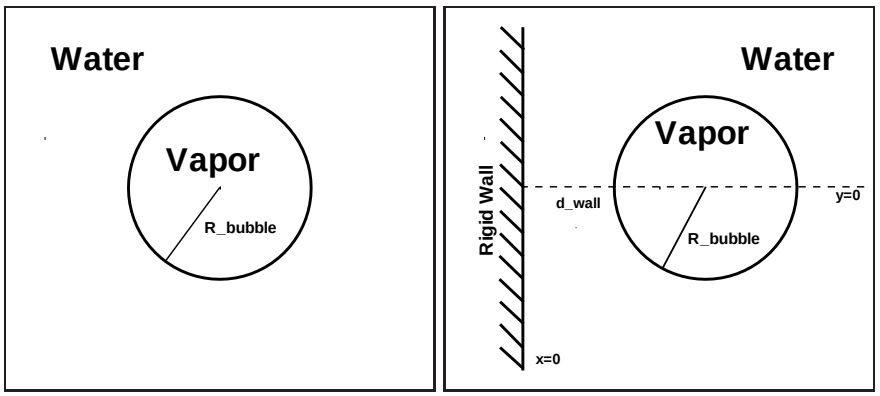

Figure 7: Bubble away (left) and next (right) to a rigid wall

stiffened gas approach in Section 2 where the liquid phase is characterized by a stiffened gas law and the vapor phase by a perfect gas law which can both be written in the form (5) where the material coefficients for the pure phases are listed in Table 1.

The governing equations are the Euler equations (1) and the non-conservative transport equations (10) for the pressure law coefficients. These are discretized by the finite volume scheme (11) and the non-conservative upwind discretization (25). The efficiency of the numerical discretization is significantly improved by the multiscale-based grid adaptation employing multilevel time stepping as summarized in Section 3.3.

Three configurations have been investigated, namely, (i) a two-phase Riemann problem (1D) to validate the numerical discretization with respect to accuracy, efficiency, reliability and robustness, (ii) a vapor-filled cylindrical bubble surrounded by water (2D) where we are interested in the influence on the stability of the bubble surface and (iii) the collapse of a vapor-filled cylindrical bubble next to a rigid wall (2D).

All computations have been performed with the code **QuadConcept** where we employ multiscale-based grid adaptation. This solver is based on the implementation of the adaptive finite volume solver originally developed for compressible single-phase fluids, cf. [Mül02]. It has been extended by the upwind discretization of the pressure law coefficients, see Section 3.2.

4.1 Two-Phase Riemann Problem

We consider a shock tube problem where initially two states corresponding to pure liquid (left) and vapor (right) are separated by a diaphragm shown in

Figure 8 (left). The initial data corresponding to state L and R taken from

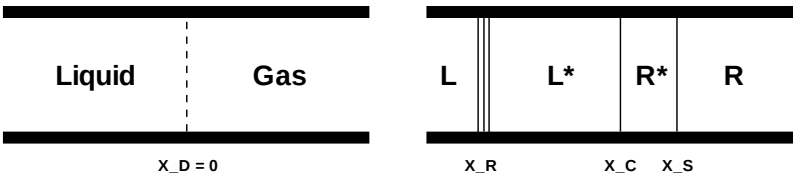

Figure 8: Shock tube problem: Initial configuration (left) and solution at some later instant (right)

[Han98], p. 41, are listed in Table 2. They are characterized by high pressure and density values in the liquid and low pressure and density values in the vapor where the temperature is chosen to be in equilibrium. These are characteristic for injection nozzles of diesel engines, cf. [DB06].

		State L	State L*	State R*	State R
		Liquid	Liquid	Gas	Gas
ϱ	[kg/m^3]	1000	978.672	0.028728	0.026077
v_x	[m/s]	0	32.998	32.998	0
p	[Pa]	5e+07	2425.7	2425.7	2118
$\varrho\, c$	[kg/m^{2}s]	1.58193e+06	1.44889e+06	9.87723	8.79338
τ	[m^3/kg]	0.001	0.00102179	34.8092	38.348
Ma	[-]	0	0.022288994	0.095975086	0
T	[K]	283	247.86	294.2	283

Table 2: Shock tube problem: Initial and intermediate states

Removing instantaneously the membrane a fast expansion wave is running into the liquid phase and a shock wave is moving into the vapor phase followed by the material interface, see Figure 8 (right). The constant intermediate states are given in Table 2. The velocities of the three waves are listed in Table 3. We note that the shock speed is only about 25 % of the velocity of the rarefaction wave.

$v_R^- = v_{R-} - c_{R-}$	$v_R^+ = v_{R+} - c_{R+}$	v_C	v_S
-1581.93	-1447.46	32.998	357.588

Table 3: Shock tube problem: Wave speeds

For this simple configuration we performed several computations. The purpose of these computations is twofold, namely, (i) to validate the implementation and the numerical discretization with respect to accuracy, robustness and reliability and (ii) to investigate the effect of higher order reconstruction, grid adaptation and multilevel time stepping on the numerical results.

The computational domain is $\Omega = [-2, 0.5]$ and the final time is $t = 1.001984 \times 10^{-3}$ [s]. The coarse grid discretization consists of $N_0 = 50$ cells. The number

of refinement levels is always $L = 8$. From this we infer that the (uniform) reference grid on level L is composed of $N_L = 12800$ cells. The time step size is determined by $\Delta t = 3.1312 \times 10^{-8}$ [s] corresponding to a CFL number of 0.25 with respect to the initial data. Hence, we perform $n = 32000$ time steps. If not stated otherwise the threshold value is $\varepsilon = 0.0001$ and we use the second order reconstruction of the primitive variables ϱ, v and p. The computations are performed employing multilevel time stepping.

Validation. In Figures 9, 10, 11, 12, 13, 14, 15, 16 the numerical results and the exact solution are shown for the final time. The exact solution of the Riemann problem was computed by the iterative solver of Colella/Glaz [CG85]. We note that the numerical results are in good agreement with the exact solution except for the temperature at the material interface. The problem on the temperature has already been reported in [SCB99].

Nevertheless there are some deficiencies that become visible only if one zooms into the solution. First of all, we observe that the numerical discretization of the pressure law coefficients leads to a smearing of the mass and volume fraction, see Figure 23 and 24, though the underlying mathematical model in Section 2 is based on the assumption of immiscibility. This numerical mass diffusion causes an overheating in the liquid and vapor phase next to the material interface, see Figure 21. In addition, we observe some effect due to the numerical mass diffusion on the Mach number in the vapor phase, see Figure 22.

Another deficiency can be observed in the pressure in the liquid phase, see Figures 31 and 37, 38, respectively. When the rarefaction wave passes we observe an over-expansion of the liquid. This effect becomes stronger with higher numerical dissipation introduced by a first order discretization, see Figure 31. For the 1st order reconstruction this numerical overheating can be observed in the entire regime between rarefaction wave and the material interface whereas for 2nd order reconstruction it only takes place near the rarefaction wave. We note that this effect becomes stronger the more cells are refined, i.e., the threshold value ε decreases. It becomes the strongest if we perform no grid adaptation at all, i.e., $\varepsilon = 0$, see Figures 37, 38. Hence this effect is caused by the numerical discretization itself rather than by grid adaptation. These observations have been confirmed by computations with the non-adaptive 1st order code developed in [Bar02, BH05].

Furthermore we note that the position of the material interface, see Figures 18, 19, 21, 22, 23, 24, and the position of the shock wave, see Figures 25, 26, 27, 28, 29, 30, differ slightly between the numerical results and the exact solution. Most significant is the difference for the specific volume at the material interface displayed in Figure 19. This is caused by the discretization of the non-conservative transport equations for the pressure law coefficients. In return, we note that pressure and velocity are constant across the material interface and no oscillations are introduced according to the construction of the upwind discretization (25), see Figures 17 and 20.

Although there are some deficiencies we want to emphasize that these effects are local and can only be observed on very small scales.

Influence of thresholding, time stepping and reconstruction. Next we investigate the influence of the higher order reconstruction on the numerical results. For this purpose we performed computations using 1st order and 2nd order reconstruction, respectively, and compared these with the exact solution. As we may conclude from Figures 25, 26, 27, 28, 29, 30 the shock wave is much

sharper resolved for 2nd order reconstruction. For 1st order reconstruction it is significantly smeared. This is important to note because we want particularly to investigate the behavior of a collapsing vapor bubble. For this purpose, it is important to well-resolve the dynamics inside the bubble. For the rarefaction wave in the liquid the influence of the higher order reconstruction is in general not as severe as for the shock wave in the vapor phase, see Figures 31, 32, 33, 34, 35, 36. There are slight improvements at the edges of the rarefaction fan. As already discussed above, the 2nd order reconstruction strongly improves the solution between the rarefaction wave and the material interface, see Figure 31. Furthermore we note that the higher order reconstruction also improves the solution at the material interface, see Figures 18, 19, 21, 22 23, 24. Here again the pressure is exceptional, see Figure 17.

Due to the strong smearing for the 1st order scheme the efficiency of the adaptive scheme is significantly reduced. To show this we performed several computations for 1st and 2nd order where we vary the threshold value ε. From Tables 4 and 5 we conclude that the number of cells is always higher for the 1st order computation. With smaller threshold value ε the number of grid cells is increasing but less strong for the 2nd order scheme. Therefore the computational times are always lower for these computations.

These observations hold true for global and multilevel time stepping. However, comparing the results in Tables 4 and 5 we note that the computational costs are always less for multilevel time stepping. As has been observed in previous investigations, cf. [MS06], less numerical diffusion is introduced because the number of time steps is reduced for the cells on coarser scales. In addition, thresholding is performed less frequently on all scales reducing the threshold error introduced in each grid adaptation step.

From the above discussion we finally conclude that grid adaptation, multilevel time stepping and higher order reconstruction significantly improve the efficiency and the accuracy of the solution.

ε	$\frac{\text{\# cells adapt. grid}}{\text{\# cells ref. grid}}$		$\frac{\text{Cpu adapt. scheme}}{\text{Cpu ref. scheme}}$	
	1st order	2nd order	1st order	2nd order
10^{-2}	0.030	0.024	0.008	0.060
10^{-3}	0.056	0.032	0.002	0.013
10^{-4}	0.098	0.047	0.054	0.020
10^{-5}	0.133	0.072	0.075	0.034
10^{-6}	0.119	0.090	0.081	0.043

Table 4: Parameter study w.r.t. threshold value and reconstruction order in case of multilevel time stepping

4.2 Planar Bubble Collapse

Next we investigate the collapse of a vapor-filled bubble embedded in a liquid surrounding far from the external boundary of the liquid, see Figure 7 (left). Here we confine to a 2D configuration that can be considered a cross-section of the radial collapse of a cylindrical bubble of infinite length. The initial states for the pure phases are the same as for the shock tube problem, see Table 2. The

ε	$\frac{\text{\# cells adapt. grid}}{\text{\# cells ref. grid}}$		$\frac{\text{Cpu adapt. scheme}}{\text{Cpu ref. scheme}}$	
	1st order	2nd order	1st order	2nd order
10^{-2}	0.036	0.026	0.031	0.025
10^{-3}	0.067	0.033	0.057	0.031
10^{-4}	0.111	0.044	0.085	0.057
10^{-5}	0.140	0.055	0.103	0.047
10^{-6}	0.166	0.078	0.114	0.059

Table 5: Parameter study w.r.t. threshold value and reconstruction order in case of global time stepping

radius of the bubble is $R = 0.001$ [m]. The midpoint of the bubble is located in the origin $\boldsymbol{x} = (0, 0)$ of the coordinate system.

For the numerical simulation we employ rotational symmetry and perform the computation only in the domain $\Omega = [0, 0.01] \times [0, 0.01]$. The coarse grid discretization consists of $N_0 = 25 \times 25$ cells. The number of refinement levels is $L = 8$. From this we infer that the (uniform) reference grid on level L is composed of $N_L = 6400 \times 6400$ cells. The time step size is determined by a fixed CFL number of 0.5. Performing $n = 230$ macro time steps this corresponds to a final time of about $t = 7.26 \times 10^{-6}$ [s]. The threshold value is $\varepsilon = 0.001$ and we use the second order reconstruction of the primitive variables ϱ, v and p. The computational domain is chosen 10 times larger than the bubble radius to avoid unphysical reflections from the boundary. Since we are not interested in the expansion wave in the water phase we do not perform grid adaptation outside a domain of radius larger than 0.002 [m]. This significantly reduces the number of cells in the far field without spoiling the accuracy of the wave processes inside the vapor bubble. The computations are performed employing multilevel time stepping. The CPU time was about 22.22 hours on a PC with AMD processor Opteron 250.

The wave structure emanating at the phase boundary is the same as for the shock tube problem, see Section 4.1, i.e., a very fast rarefaction wave is running into the water and a less fast shock wave is running into the vapor, respectively. The phase boundary is following the shock wave firstly at low speed that leads to a shrinking of the vapor bubble. At the same time the shrinking is continuously accelerated and causes compression waves in the bubble. To illustrate the dynamic behavior of the bubble collapse we extract for each macro time step the data along the x-axis and store them in one file. From this we then visualize the flow along this axis in time, see Figures 39, 40, 41, 42, 43, 44.

The shock wave is focusing in the bubble center at time 2.65×10^{-6} [s] where it is reflected. The average speed of the shock wave is about 377 [m/s]. This is almost the sound speed corresponding to the initial vapor data, i.e., there has been no significant heating of the vapor by the first inwards running shock. But during the shrinking process temperature increases.

The reflected shock wave is running towards the phase boundary. At time 4.27×10^{-6} [s] the shock wave is interacting with the phase boundary at radial position $r = 0.0006$ [m]. From this we deduce an average shock speed of 373 [m/s]. Due to the high difference in the acoustic impedance, see Table 2 state L^* and R, a weak shock is transmitted into the water phase whereas a

stronger shock wave is reflected and running back again towards the bubble center cf. [Hen70, Tho72]. The bubble still continues shrinking.

The processes of shock focusing and reflecting in the bubble center and the interaction of the reflected shock wave with the phase boundary is repeating at least four times. Due to the shrinking process and compression by the shock waves the vapor is significantly heated. Finally at time 6.67×10^{-6} [s] the bubble reaches its minimal radius of about $R_{min} = 3.93 \times 10^{-5}$ [m]. Note that due to the finite resolution of the discretization not all effects can be resolved in detail. The number of shock focusing processes depends on the initial bubble radius and the exterior pressure in the liquid.

In Figure 39 the temporal variation of the Mach number distribution is shown. We note that the phase boundary is accelerated from subsonic speed Ma=0.01, see Table 2, to supersonic speed Ma = 1.22, i.e, $v_{vapor} > 555$ [m/s]. As can be deduced from the zoom in Figures 41, 42, 43 and 44 another shock is forming at the bubble in the instant of the largest acceleration and running into the liquid. According to Hanke, see [Han98], p. 41, this shock wave is caused by the strong acceleration of the phase boundary which comes at rest when the bubble reaches its smallest radius and becomes accelerated later on in outward direction.

In Table 6 we summarize the extremal data of certain physical quantities in the instant of the bubble collapse. In many publications concerning bubbly

		units	Vapor
minimal radius	R_{min}	[m]	3.93×10^{-5}
maximal pressure	p_{max}	[Pa]	1.09×10^{9}
maximal density	ϱ_{max}	[kg/m^3]	2.32×10^{3}
maximal temperature	T_{max}	[K]	8.27×10^{3}
maximal velocity	v_{max}	[m/s]	2000
maximal Mach number of bubble contour	Ma	[-]	1.22

Table 6: Quasi-1D Bubble Collapse: Final states after collapse inside vapor bubble

liquids the liquid is assumed to be incompressible. At the instant of the bubble collapse we find for the pressure in the liquid 1.09×10^9 [Pa]. At these high values the incompressibility assumption is no longer justified.

Since in our model the two phases are characterized by the volume and mass fraction the phases are not strictly separated. Due to numerical dissipation introduced by the underlying finite volume discretization the phases will be mixing near the phase boundary causing some numerical phase transition. As can be depicted from Figure 40 the numerical phase transition zone is small in the bubble collapse process. However when the bubble starts growing again a significant phase transition layer is forming. This does not occur in the results by Hanke due to the fitting of the phase boundary.

We emphasize that the above observations and conclusions are in agreement with the results reported in [Han98] for the same configuration. However there have been differences in the physical modeling and the numerical discretization. Hanke developed the finite volume code BUB for the spherical and cylindrical

bubble collapse based on the Navier-Stokes equations using different equations of state for the vapor phase, e.g., perfect gas, van der Waals and others, [HB98, Han98]. The material interface is fitted separating the liquid and vapor phase, respectively. In each subdomain the fluid equations are solved where viscosity and heat conduction are taken into account in the gas phase but neglected in the liquid. The material interface is numerically treated according to [CSL96] using front tracking. Thereby mixing of the phases near the phase boundary is suppressed.

To validate the 2D computations we have performed computations with the quasi-onedimensional code BUB using 200 cells in the gas and 800 cells in the liquid neglecting dissipative effects as well as surface tension. In Figure 45 we compare the Mach number distribution for both computations. The wave pattern is identical. However, the bubble collapse is faster in our 2D computation due to the higher acceleration of the interface after the first interaction with the shock wave, cf. $Ma_{max} = 1.2$ (2D) and $Ma_{max} = 0.8$ (BUB). This is due to the higher resolution of the gas phase by BUB which is fixed because the grid in the two phases is attached to the interface and the grid points are redistributed after each time step. For our 2D computation the number of cells is significantly reduced with shrinking bubble radius. Taking this into account the results can be considered in qualitatively good agreement.

The lack of viscosity and heat conduction in the present paper may significantly affect the states in the instant of shock focusing in the bubble center. According to the similarity solution derived by Guderley [Gud42] for spherical compression waves where viscosity is neglected the pressure might increase asymptotically to infinity. Due to the finite resolution in the discretization the pressure will be bounded in the computation but it will further increase with higher resolution. Taking into account viscosity the pressure will stay bounded even with increasing resolution. This has been confirmed numerically in [Han98].

4.3 Planar Bubble Collapse next to a Rigid Wall

Finally we investigate the bubble collapse for initial conditions as in Section 4.2, see Table 2, but next to a rigid plane wall, see Figure 7 (right), i.e., the axis of the cylindrical bubble is parallel to the rigid wall and again it is possible to consider a plane problem. The bubble radius is $R = 0.001$ [m] and the bubble center is located at $\boldsymbol{x} = (3R/2, 0)$, i.e., the distance of the bubble to the planar wall ($x = 0$) is $d = R/2$.

The computational domain is determined by $\Omega = [0, 0.1] \times [-0.05, 0.05]$. The coarse grid discretization consists of $N_0 = 25 \times 25$ cells. The number of refinement levels is $L = 8$. From this we infer that the (uniform) reference grid on level L is composed of $N_L = 6400 \times 6400$ cells. The time step size is determined by a fixed CFL number of 0.5. Performing $n = 60$ macro time steps this corresponds to a final time of about $t = 1.81 \times 10^{-5}$ [s]. The threshold value is $\varepsilon = 0.001$ and we use the second order reconstruction of the primitive variables ϱ, v and p. To avoid unphysical reflections from the boundary of the computational domain its distance is chosen 100 times the bubble radius. Since we are not interested in the flow field far away from the wall we do not perform grid adaptation outside a radius larger than 0.002 [m] around the initial bubble center. The computations are performed employing multilevel time stepping with 60 macro time steps. The CPU time was about 11.5 hours on a PC with

AMD processor Opteron 250.

The dynamics of the waves developing in the fluid and their interaction with the wall and the bubble interface can be deduced from the plots of the density gradient magnitude, see Figures 46, ...,51 and 52, 54, ...,110. Due to the different scales involved in the liquid and in the vapor these have to be scaled logarithmically to show them simultaneously in one picture, i.e., we present $\log(1 + |\nabla \varrho|)$ where the density gradient magnitude is shifted by 1 to account for vanishing gradients. Due to the waves and their interactions the fluid is accelerated. This highly dynamic process is visualized by integral curves of the velocity shown in Figures 53, 55, ...,111 corresponding to the same times as for the density gradient magnitude. The figures for both quantities are superposed with contour lines of the vapor fraction to see how the phase interface is affected by the wave interaction process.

First of all, we focus on the waves in the liquid, see Figures 46, ...,51. In the early stage of the computation the wave structure developing at the phase boundary is the same as for the bubble collapse, see Section 4.2. An expansion wave $R1$ is running into the liquid, see Figure 46. Since the bubble is located next to a rigid wall the expansion wave R1 is reflected as an expansion wave R2 at the wall, see Figure 47. Due to the strong expansion the liquid behind the wave R2 the pressure drops below zero and a cavitation is forming. The reflected expansion wave $R2$ again is reflected at the phase boundary, see Figure 48. Due to the low acoustic impedance in the gas and the high acoustic impedance in the liquid, see [Hen70, Tho72], the reflected wave is a compression wave, i.e., the phase is inverted. This procedure of reflection at the wall and at the phase boundary is continued, see Figures 49, ...,51 where the phase is maintained at the wall but is inverted at the bubble.

To see the effect of the reflected expansion and compression waves on the vapor phase inside the bubble we zoom into the vapor bubble, see Figures 52, ...,111. In the beginning, there is only a shock wave S running towards the bubble center, see Figure 52. When the reflected expansion wave R2 is interacting with the phase boundary, see Figure 54, then it is partially reflected into the liquid as discussed before and partially transmitted into the vapor phase, see R3 and T1 in Figure 56. We note that the waves are running faster in the liquid than in the vapor due to the higher sound speed in the liquid. Due to the curvature of the bubble contour, the transmitted waves in the vapor are defracted, see Figures 56, 58, ...,68. Therefore the transmitted waves, see for instance T1 in Figures 56, 58, ...,74, have the shape of a convex lens fixed at the phase boundary, see Figures 58 and 60. With increasing time the curvature of the lens becomes stronger, see Figures 62, 64, ...,68, and, finally, the lens closes to a circle, see Figure 70. The now circular wave focuses inside the bubble at the symmetry line and is reflected, see Figures 72 and 74. Note that by the transmitted waves the distribution inside the bubble becomes strongly heterogeneous resulting in a pressure gradient of low pressure left to the bubble center and high pressure to the right.

Simultaneously, the shock wave S is focusing in the bubble center, see Figure 66, and is reflected there. The reflected shock wave RS1 is running in outward direction towards the bubble interface, see Figures 68, 70, 72, 74. The shock wave is interacting with the transmitted waves. Since in the vapor the difference of the acoustic impedance is small these waves are transmitting without causing reflection waves. Due to the defraction of the expansion and compression waves

the initially circular shock front flattens at the top and the bottom side and becomes wavy, see Figure 74. The reflected shock wave RS1 is interacting with the bubble interface. Due to the high difference in the acoustic impedance in the two phases it is being reflected there and running inwards again, see RS2 in Figures 76 and 78. This shock wave focuses and is reflected again as shock wave RS3, see Figure 80. This process of shock focusing and shock reflection at the phase boundary is continued. The details of this process can not be presented here.

Due to the wave processes in the liquid and in the vapor the flow field is accelerated. The dynamics of the acceleration can be depicted from the integral curves of the velocity presented in Figures 53, 55, ...,111. Starting from a flow at rest the flow field is accelerated towards the bubble center when the expansion wave R1 and the shock wave S pass, see Figure 53. The velocity field is rotational symmetric as long as the expansion wave R1 has not been reflected at the wall. The reflection of wave R1 leads to a distortion of the symmetry. Behind the reflected expansion wave R2 a low pressure regime develops that extends with increasing time into the far field. Therefore, the liquid is accelerated in the direction of the symmetry line and near the wall it is moving almost parallel to the wall. At the symmetry line the liquid is then deflected and directed towards the vapor bubble, see Figures 55, 57, ...,89. While the flow is deflected near the wall, the flow away from the wall is directed towards the bubble center, see Figures 55, 57, ...,61. Inside the bubble the vapor is no longer moving towards the bubble center when the transmitted waves, see for instance T1, pass but is deflected towards the symmetry line. When the shock wave S focuses in the bubble center, see Figure 67, it is reflected there and the flow behind the reflected shock wave RS1 is now accelerated in outward direction, see Figures 69, 71, 73, 75. However, this acceleration is not sufficient to revert the flow direction due to the underlying velocity field caused by the inward running shock S and due to the pressure gradient caused by the transmitted expansion waves as discussed above. Therefore the vapor in the right part of the bubble is still moving inwards. On the other hand, behind the transmitted waves, see for instance T1, the vapor is accelerated towards the bubble center, see Figures 65 and 67. Due to the strong acceleration of the vapor behind the reflected shock wave RS1, the vapor behind the transmitted waves is repelled, see Figures 69, 71, 73, 75. A front is forming where the vapor from both sides is deflected towards the symmetry line where the integral curves of the velocity coincide in a stagnation point. Since the vapor is stronger accelerated at the right side of the deflection front than at the left side, the stagnation point is moving towards the wall, see Figures 77, 79, 81, 83, 85. Due to the ongoing process of shock wave focusing in the bubble and shock reflection at the phase boundary, the underlying flow field is further accelerated without changing the overall flow direction in the regions left and right from the deflection front. However, the flow attached to this front changes its direction. In the beginning, the attached flow is directed towards the stagnation point, see Figures 71, 73, ...,83, whereas it is moving away from the stagnation point in outward direction at some later time, see Figure 85. Since the vapor is stronger accelerated to the right of the deflection front than to the left, a velocity gradient develops across the front. Due to this velocity gradient two vortices are forming inside the vapor bubble above and below the symmetry line, rotating clockwise and counter-clockwise, respectively, see Figures 83, 85, 87, 89, 91. The rotation of the vortices causes

the vapor to concentrate in the center of the vortices. This results in a high compression of the vapor. In the core of the vortices we compute a pressure of about 300 [bar], a density of about 250 [kg/m^3] and a temperature of about 600 [K]. When the vapor mass is concentrating in the core of the vortices, the vapor bubble splits into two parts and a liquid jet is forming, see Figures 91, 93, 95, 97, 99. This jet is directed towards the wall due to the clockwise and counter-clockwise rotation of the vortices above and below the symmetry line, respectively, see Figure 93. The two vapor bubbles cause a bottleneck for the liquid due to the high density of the vapor. Therefore the liquid is accelerated towards the wall through this orifice, see Figures 113, 115, ...,123. The maximal speed of about 900 [m/s] is reached at time $t = 9.07 \times 10^{-6}$ [s], see Figure 119, at the symmetry line between the two vortices. This value corresponds to a Mach number of 1.6. At this instant, the vapor is at rest in the center of the vortices whereas the velocity is about 300 [m/s] directed away from the wall at the farest point of the bubble contours from the symmetry line.

When the liquid is accelerated through the orifice the pressure is increasing before the bottleneck resulting in a high pressure region of about 2400 [bar], see Figure 116. Since the liquid is expanding behind the orifice the high pressure region is squeezed through this bottleneck and shot like a projectile towards the wall where it hits with high pressure that is about 5 times that of the undisturbed liquid, see Figures 116, 118, 120, 122. The impact of the high pressure might be the cause of material damage as has been observed in experiments, cf. [PL98, BNSV01a, BNSV01b].

When the liquid jet hits the wall another stage in the bubble collapse begins. The water supplied by the jet is deflected to both sides of the symmetry axis due to the resistance of the wall. Since this liquid is moving at higher speed than the liquid supplied from the undisturbed flow, it represses the latter, see Figures 93, 95, 97, 99. Because of this process the two vortices and attached to these the vapor bubbles start to move towards the wall where they are deflected in upward and downward direction, see Figures 101, 103, ...,111. If the high temperature vapor bubbles would come into contact to the wall it might cause some material damage. However, in our computations the vapor bubbles are surrounded by a phase transition zone where the temperature is decreasing significantly.

We conclude the numerical investigation by some comments on the phase interface. Due to the stiffened gas model, the phase boundary is not necessarily a sharp discontinuity but may become diffusive. In the beginning, the interface is slightly accelerated by the shock wave S resulting in a slow shrinking process of the vapor bubble, see Figures 52, 54, ...,74. When the shock wave RS2 is reflected at the phase interface, the phase boundary is significantly accelerated, see Figures 76, 78, 80. Due to the inertia of the liquid a phase transition zone develops filled with a mixture of gas and liquid, see Figures 82, 84, ...,110. By the vortices forming inside the vapor bubble, the pure vapor is transported to the core of these vortices. In Figures 84 and 86 we see that the vapor fraction contour corresponding to pure vapor starts bulging and is finally penetrated by the vapor-liquid mixture, see Figures 90 and 92. In the end, only two bubbles filled with pure vapor remain, see Figures 94, 96, ...,110.

5 Conclusion

The stiffened gas model of Saurel and Abgrall [SA99] has been successfully extended to a higher order scheme on locally refined grids. Multiscale-based grid adaptation techniques [Mül02, CKMP03] have been employed to improve the efficiency of the scheme. This allows for a locally high resolution that is needed to resolve accurately the local physical effects in the bubble collapse process. Since this process is highly dynamical the time discretization is explicit. Therefore the CFL condition is very restrictive because of the small cells sitting on the high refinement levels. For the cells on the coarser discretization levels we use a multilevel time stepping strategy that allows for larger time steps on coarser scales. This has been recently developed in combination with the multiscale-grid adaptation, cf. [MS06, LMS05, LMMS06]. This strategy had to be modified taking into account the non-conservative upwind discretization of the evolution equations for the material parameters.

The accuracy and the efficiency of the resulting adaptive scheme has been validated by means of a two-phase Riemann problem. It turned out that the accuracy is significantly improved by the 2nd order reconstruction in comparison with the original scheme of Saurel and Abgrall that is of 1st order only. In addition, the CPU time as well as the memory resources are tremendously reduced because of the grid adaptation and the multilevel time stepping strategy. However, the non-conservative discretization of the evolution equations for the material parameters results in some slight deviation of the shock position from the exact position. Moreover, an additional temperature jump can be observed in the numerically smeared contact discontinuity. For inviscid computations, this has no effect on the computation. But for computations including viscosity it might become significant in case the viscosity coefficient is temperature dependent.

The scheme has then been applied to investigate the collapse of a free planar vapor bubble at low pressure and density surrounded by water at high density and pressure. A shock wave is running inside the vapor bubble between bubble center and phase boundary where it is focusing and reflected several times. By this process the gas undergoes a strong compression resulting in a significant heating. The phase boundary is accelerated towards the bubble center where it collapses and reaches a minimal radius that is about 25 times smaller than the original bubble radius. In the instant of the collapse a shock wave is running into the water that results in a significant compression of the liquid. At these high values the incompressibility assumption is no longer justified. Due to the compression inside the bubble, density, pressure and temperature increase by several orders of magnitude. For more realistic values the gas should be modeled by a real gas equation of state rather than the perfect gas law. We emphasize that these observations and conclusions are in agreement with the results reported in [Han98, HB98] for the same configuration but performing quasi-1D computations exploiting spherical symmetry.

Finally we investigate the bubble collapse next to a rigid wall. The dynamics of the resulting flow field can be separated into three stages. In a first stage, a low pressure regime is developing between the wall and the vapor bubble. This is caused by expansion and compression waves running between the wall and the bubble where they are reflected. Due to the low acoustic impedance in the gas and the high acoustic impedance in the liquid, the phase is inverted when

the wave is reflected at the bubble contour but it remains unchanged when it is reflected at the wall. At the same time, a shock wave is running inside the bubble towards the bubble center. Due to transmitted expansion and compression waves at the interface, the pressure distribution becomes asymmetric also inside the bubble. When the shock wave focuses in the bubble center a second stage starts where a liquid jet is forming that penetrates the bubble at the symmetry line and is directed towards the wall. This process is caused by the formation of two vortices inside the vapor bubble by which the vapor is concentrating in two almost rotational symmetric vapor bubbles above and below the symmetry axis. The small distance between the two vortices causes a bottleneck for the liquid which acts as a nozzle where the liquid is significantly accelerated. In front of this bottleneck a high pressure zone is forming in the liquid where the pressure is about 5 times higher than in the undisturbed liquid. This high pressure liquid is then squeezing through the bottleneck and directed towards the wall where it hits with high pressure. The impact of the high pressure might be the cause of material damage. But this analysis requires considering of the coupled fluid-structure problem with the appropriate modeling of elastic-plastic stress waves in the solid wall, see [Dic97, Spe00]. When the jet hits the wall, the third stage of the flow process starts. The liquid supplied by the jet is deflected at the wall to both sides of the symmetry axis and pushes away the water supplied from the free stream from above and below. In the wake of the jet the system of the splitted bubbles and the vortices start moving towards the wall where they are deflected upward and downward the symmetry axis.

The numerical investigation clearly indicate that the bubble splitting and the formation of the liquid jet is essentially caused by the acceleration of the vapor inside the bubble due to the shock wave focusing in the center and its reflection at the phase interface as well as its interaction with the transmitted compression and expansion waves. Therefore the frequently made assumption of a homogeneous state inside the vapor bubble can no longer be considered to be admissible.

So far viscosity and heat conduction as well as surface tension have not been taken into account. These might affect the processes of bubble collapsing, jet formation and bubble splitting. Furthermore, the phase boundary is diffusive due to the modeling of the two-phase fluid by a single compressible medium. It would be interesting to compare the results with sharp interface model using level set methods, cf. [NDT06]. This, in particular, would allow to use different models for the gas and the liquid, respectively.

Acknowledgment

The authors would like to thank Dr. Sigrid Andreae (MAN Augsburg, Germany) and Dr. Gerd Britten (BMW Munich, Germany) for their assistance in visualizing the numerical results and providing the computations by the BUB code.

References

[Abg88] R. Abgrall. Generalisation of the Roe scheme for the computation of mixture of perfect gases. *Recherche Aérospatiale*, 6:31–43, 1988.

[Abg96] R. Abgrall. How to prevent pressure oscillations in multicomponent flow calculations: A quasi-conservative approach. *J. Comp. Phys.*, 125:150–160, 1996.

[ABM05] S. Andreae, J. Ballmann, and S. Müller. Wave processes at interfaces. In G. Warnecke, editor, *Analysis and numerics for conservation laws*, pages 1–25. Springer, Berlin, 2005.

[ADH98] F. Arandiga, R. Donat, and A. Harten. Multiresolution based on weighted averages of the hat function I: Linear reconstruction techniques. *SIAM J. Numer. Anal.*, 36(1):160–203, 1998.

[AK01a] R. Abgrall and S. Karni. Computations of compressible multifluids. *J. Comp. Phys.*, 169(2):594–623, 2001.

[AK01b] R. Abgrall and S. Karni. Ghost-fluids for the poor: A single fluid algorithm for multifluids. In H. Freistühler and G. Warnecke, editors, *Hyperbolic Problems: Theory, Numerics, Applications*, pages 1–10. Birkhäuser Verlag, 2001.

[And07] S. Andreae. *Wave Interactions with Material Interfaces.* PhD thesis, RWTH Aachen, 2007.

[Bar02] Th. Barberon. *Modélisation mathématique et numérique de la cavitation dans les écoulements multiphasiques compressibles.* PhD thesis, Université de Toulon et du Var, 2002.

[BE66] T.B. Benjamin and A.T. Ellis. The collapse of cavitation bubbles and the pressure thereby produced against solid walls. *Phil. Trans. R. Soc. Lond. A*, 260:221–240, 1966.

[BH05] T. Barberon and Helluy. Finite volume simulation of cavitating flows. *Computers and Fluids*, 34(7):832–858, 2005.

[BHR03] T. Barberon, P. Helluy, and S. Rouy. Practical computation of axisymmetrical multifluid flows. *International Journal of Finite Volumes*, 1(1):1–34, 2003.

[BKZ92] J.U. Brackbill, D.B. Kothe, and C. Zemach. A continuum method for modeling surface tension. *J. Comp. Phys.*, 100:335–354, 1992.

[BLM04] F. Bramkamp, Ph. Lamby, and S. Müller. An adaptive multiscale finite volume solver for unsteady and steady state flow computations. *J. Comp. Phys.*, 197(2):460–490, 2004.

[BNSV01a] E.-A. Brujan, K. Nahen, P. Schmidt, and A. Vogel. Dynamics of laser–induced cavitation bubbles near an elastic boundary. *J. Fluid. Mech.*, 433:251–281, 2001.

[BNSV01b] E.-A. Brujan, K. Nahen, P. Schmidt, and A. Vogel. Dynamics of laser–induced cavitation bubbles near elastic boundaries: Influence of the elastic modulus. *J. Fluid. Mech.*, 433:283–314, 2001.

[CDP96] J. M. Carnicer, W. Dahmen, and J. M. Peña. Local decomposition of refinable spaces and wavelets. *Appl. Comput. Harmon. Anal.*, 3:127–153, 1996.

[CG85] Ph. Colella and H.M. Glaz. Efficient solution algorithms for the Riemann problem for real gases. *J. Comp. Phys.*, 59:264–289, 1985.

[CGM+86] I.-L. Chern, J. Glimm, O. McBryan, B. Plohr, and S. Yaniv. Front tracking for gas dynamics. *J. Comp. Phys.*, 62:83–110, 1986.

[CKMP03] A. Cohen, S.M. Kaber, S. Müller, and M. Postel. Fully Adaptive Multiresolution Finite Volume Schemes for Conservation Laws. *Math. Comp.*, 72(241):183–225, 2003.

[CKP01] A. Cohen, S.M. Kaber, and M. Postel. Multiresolution analysis on triangles: application to gas dynamics. In H. Freistühler and G. Warnecke, editors, *Hyperbolic Problems: Theory, Numerics, Applications*, pages 257–266. Birkhäuser Verlag, 2001.

[CS97] J.-P. Cocchi and R. Saurel. A Riemann problem based method for the resolution of compressible multimaterial flows. *Journal of Computational Physics*, 137(2):265–298, 1997.

[CSL96] J.P. Cocchi, R. Saurel, and J.C. Loraud. Treatment of interface problems with Godunov-type schemes. *Shock Waves*, 5:347–357, 1996.

[DB06] C. Dickopp and J. Ballmann. Two-phase flow through injection nozzles. In F. Asakura, H. Aiso, S. Kawashima, A. Matsumura, S. Nishibata, and K. Nishihara, editors, *Hyperbolic Problems: Theory, Numerics, Applications*, pages 351–358. Yokohama Publishers, Japan, 2006.

[DGP98] R. DiLisio, E. Grenier, and M. Pulvirenti. On the convergence of the SPH method. *Comp. and Math. Appl.*, 35:95–108, 1998. Special Issue devoted to Simulation Method in Kinetic Theory.

[Dic97] Ch. Dickopp. *A Navier-Stokes Solver for the Simulation of Collapsing Cavitation Bubbles near to elastic Surfaces of Solids.* PhD thesis, RWTH Aachen, 1997. (in German).

[FAMO99] R.P. Fedkiw, T. Aslam, B. Merriman, and S. Osher. A non-oscillatory Eulerian approach to interfaces in multimaterial flows (the ghost fluid method). *J. Comp. Phys.*, 152(2):457–492, 1999.

[FAX01] R.P. Fedkiw, T. Aslam, and S. Xu. The ghost fluid method for deflagration and detonation discontinuities. *J. Comp. Phys.*, 154:393–427, 2001.

[GHS03] T. Gallouët, J.-M. Hérard, and N. Seguin. A hybrid scheme to compute contact discontinuities in one-dimensional Euler systems. *M2AN. Mathematical Modelling and Numerical Analysis*, 36(6):1133–1159, 2003.

[Gud42] G. Guderley. Starke kugelige und zylindrische Verdichtungsstöße in der Nähe des Kugelmittelpunktes bzw. der Zylinderachse. *Luftfahrtforschung*, 19:302–312, 1942.

[Han98] M. Hanke. Analysis and Evaluation of Physical Models for Large Variation of State in Collapsing Bubbles, 1998. Master thesis, RWTH Aachen. (in German).

[Har94] A. Harten. Adaptive multiresolution schemes for shock computations. *J. Comp. Phys.*, 115:319–338, 1994.

[Har95] A. Harten. Multiresolution algorithms for the numerical solution of hyperbolic conservation laws. *Comm. Pure Appl. Math.*, 48(12):1305–1342, 1995.

[HB98] M. Hanke and J. Ballmann. Strong changes of state in collapsing bubbles. *ZAMM*, 78:453–454, 1998. Suppl. 1.

[Hen70] L.F. Henderson. On shock impedance. *J. Fluid Mech.*, 40:719–735, 1970.

[HEOC87] A. Harten, B. Engquist, S. Osher, and S.R. Chakravarthy. Uniformly high order accurate Essentially Non–Oscillatory Schemes III. *J. Comp. Phys.*, 71:231–303, 1987.

[HN79] C. Hirt and B. Nichols. VOF method for the dynamics of free boundaries. *J. Comp. Phys.*, 39:201–225, 1979.

[Hym86] J. Hyman. Moving mesh methods for partial differential equations. *Mathematics Applied to Science*, pages 129–153, 1986.

[Kar94] S. Karni. Multicomponent flow calculations by a consistent primitive algorithm. *J. Comp. Phys.*, 112(1):31–43, 1994.

[KP91] Ch. Klingenberg and B. Plohr. An introduction to front tracking. In *Multidimensional hyperbolic problems and computations, Proc. IMA Workshop, Minneapolis/MN (USA) 1989, IMA Vol. Math. Appl. 29, 203-216* . 1991.

[LMMS06] Ph. Lamby, R. Massjung, S. Müller, and Y. Stiriba. Inviscid flow on moving grids with multiscale space and time adaptivity. In A. Bermudez de Castro, D. Gomez, P. Quintela, and P. Salgado, editors, *Numerical Mathematics and Advanced Applications: Proceedings of Enumath 2005 the 6th European Conference on Numerical Mathematics and Advanced Mathematics*, pages 755–764. Springer, 2006.

[LMS05] Ph. Lamby, S. Müller, and Y. Stiriba. Solution of shallow water equations using fully adaptive multiscale schemes. *Int. J. Numer. Methods Fluids*, 49(4):417–437, 2005.

[Mon94] J. Monaghan. Simulating free surface flows with SPH. *J. Comp. Phys.*, 110:399–406, 1994.

[MS06] S. Müller and Y. Stiriba. Fully adaptive multiscale schemes for conservation laws employing locally varying time stepping. *Journal of Scientific Computing*, 2006. online first DOI 10.1007/s10915-006-9102-z.

[Mül93] S. Müller. *Extension of ENO-procedures to two space dimensions and application to hypersonic stagnation point problem.* PhD thesis, RWTH Aachen, 1993. (in German).

[Mül02] S. Müller. *Adaptive Multiscale Schemes for Conservation Laws*, volume 27. Springer Berlin, 2002. Lecture Notes in Computational Science and Engineering.

[NDT06] R.R. Nourgaliev, T.N. Dinh, and T.G. Theofanous. Adaptive characteristics-based matching for compressible multifluid dynamics. *J. Comp. Phys.*, 213:500–529, 2006.

[NE61] C.F. Naudé and A.T. Ellis. On the mechanism of cavitation damage by nonhemispherical cavities collapsing in contact with a boundary. *Trans. ASME D: J. Basic Engng*, 83:648–656, 1961.

[OF01] S. Osher and R.P. Fedkiw. Level set methods: An overview and some recent results. *J. Comp. Phys.*, 169:463–502, 2001.

[OI03] C.D. Ohl and R. Ikink. Shock-wave-induced jetting of micron-size bubbles. *Phys. Rev. Lett. Vol.*, 90, 2003. 214502-1–4.

[OW03] C.D. Ohl and B. Wolfrum. Detachment and sonoporation of adherent hela-cells by shock wave-induced cavitation. *Biochimia Biophysica Acta*, 1624:131–138, 2003.

[PL98] A. Philipp and W. Lauterborn. Cavitation erosion by single laser-produced bubbles. *J. Fluid Mech.*, 361:75–116, 1998.

[Ray17] Lord Rayleigh. On the pressure developed in a liquid during the collapse of a spherical cavity. *Phil. Mag.*, 34:94–98, 1917.

[RS02] O. Roussel and K. Schneider. A fully adaptive multiresolution scheme for 3D reaction–diffusion equations. In B. Herbin, editor, *Finite Volumes for Complex Applications.* Hermes Science, Paris, 2002.

[RSTB03] O. Roussel, K. Schneider, A. Tsigulin, and H. Bockhorn. A conservative fully adaptive multiresolution algorithm for parabolic PDEs. *J. Comp. Phys.*, 188(2):493–523, 2003.

[SA99] R. Saurel and R. Abgrall. A simple method for compressible multifluid flows. *SIAM J. Sci. Comput.*, 21(3):1115–1145, 1999.

[SAB+99] M. Sussman, A.S. Almgren, J.B. Bell, P. Colella, L.H. Howell, and M.L. Welcome. An adaptive level set approach for incompressible two-phase flows. *J. Comp. Phys.*, 148:81–124, 1999.

[SCB99] R. Saurel, J.P. Cocchi, and P.B. Butler. A numerical study of cavitation in the wake of a hypervelocity underwater projectile. *AIAA Journal of Propulsion and Power*, 15(4):513–522, 1999.

[Set96] J.A. Sethian. *Level Set Methods.* Cambridge Monographs on Applied and Computational Mathematics, 1996.

[Spe00] U. Specht. *Numerical Simulation of Mechanical Waves at Fluid-Solid-Interfaces.* PhD thesis, RWTH Aachen, 2000. (in German).

[SSO94] M. Sussman, P. Smereka, and S. Osher. A level set approach for computing solutions to incompressible two-phase flows. *J. Comp. Phys.*, 114:146–159, 1994.

[Sus03] M. Sussman. A second order coupled level set and volume-of-fluid method for computing growth and collapse of vapor bubbles. *J. Comp. Phys.*, 187:110–136, 2003.

[Tho72] P.A. Thompson. *Compressible Fluid Dynamics.* McGraw-Hill, 1972.

[Wes87] H. Westenberger. *On the Dynamics of Momentum Transport in Bubbly Compressible Liquids.* PhD thesis, RWTH Aachen, 1987. (in German).

[WHSD] J. Welch, F. Harlow, J. Shannon, and B. Daly. The MAC method — a computing technique for solving viscous incompressible transient fluid-flow problems involving free surfaces. Report, Los Alamos Scientific Laboratory of the University of California.

[WK05] J. Wackers and B. Koren. A fully conservative model for compressible two-fluid flow. *Int. J. Numer. Methods Fluids*, 47(10-11):1337–1343, 2005.

6 Figures

6.1 Two-Phase Riemann Problem

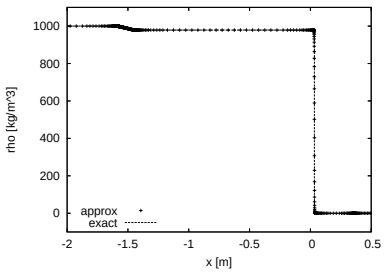

Figure 9: Density

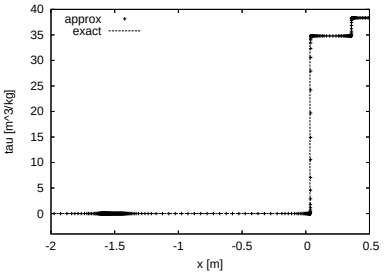

Figure 10: Specific volume

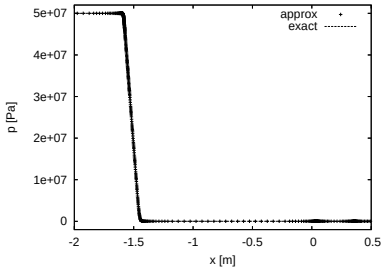

Figure 11: Pressure

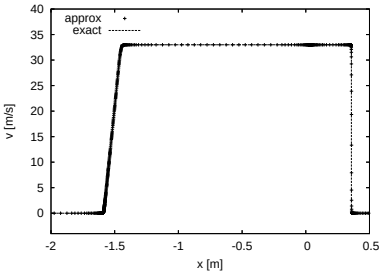

Figure 12: Velocity

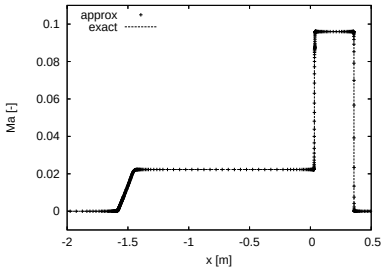

Figure 13: Mach number

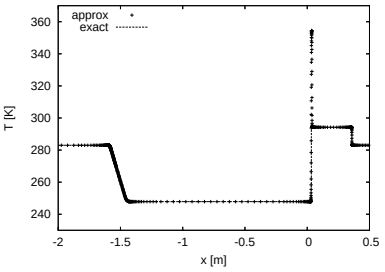

Figure 14: Temperature

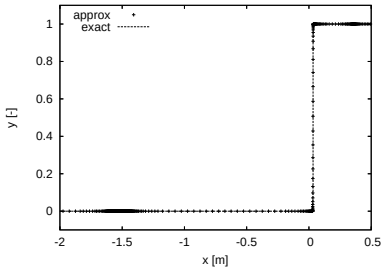

Figure 15: Vapor mass fraction

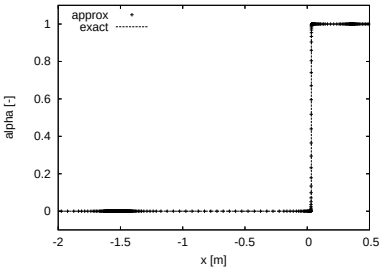

Figure 16: Vapor volume fraction

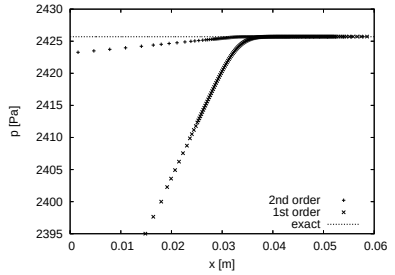

Figure 17: Pressure: Contact

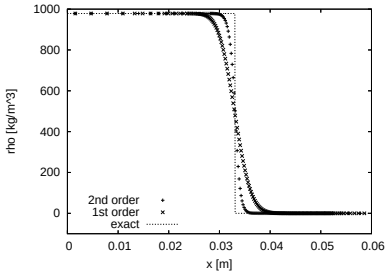

Figure 18: Density: Contact

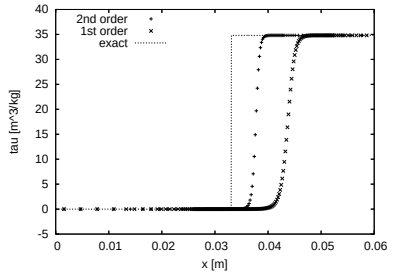

Figure 19: Spec. volume: Contact

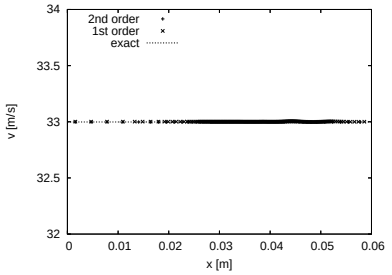

Figure 20: Velocity: Contact

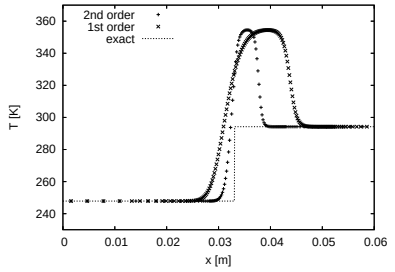

Figure 21: Temperature: Contact

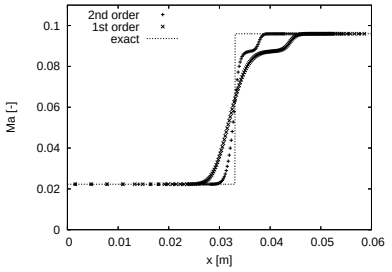

Figure 22: Mach: Contact

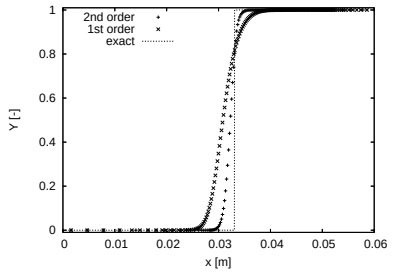

Figure 23: Mass fraction: Contact

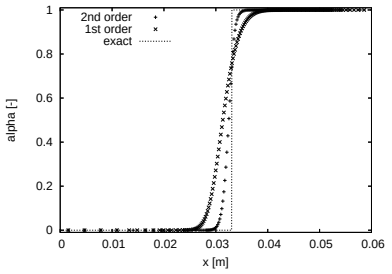

Figure 24: Volume fraction: Contact

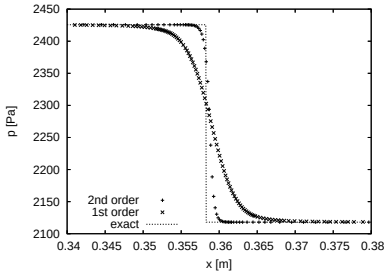

Figure 25: Pressure: Shock

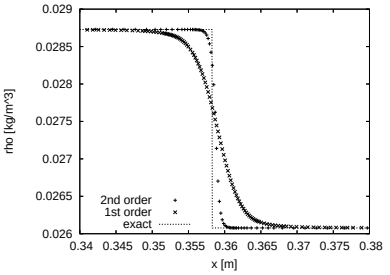

Figure 26: Density: Shock

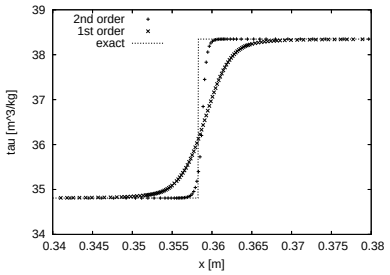

Figure 27: Spec. volume: Shock

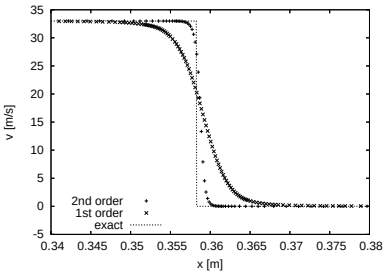

Figure 28: Velocity: Shock

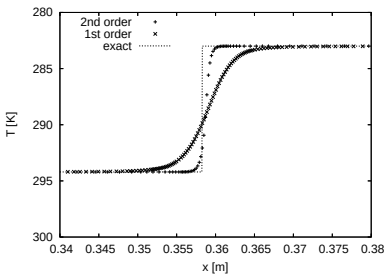

Figure 29: Temperature: Shock

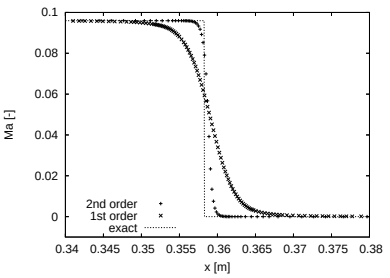

Figure 30: Mach: Shock

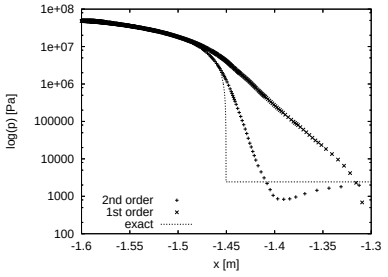

Figure 31: Pressure: Rarefaction

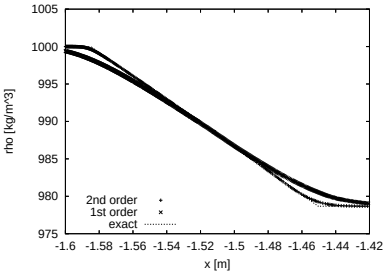

Figure 32: Density: Rarefaction

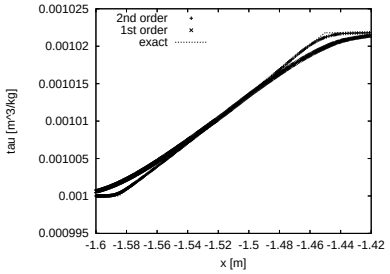

Figure 33: Spec. volume: Rarefaction

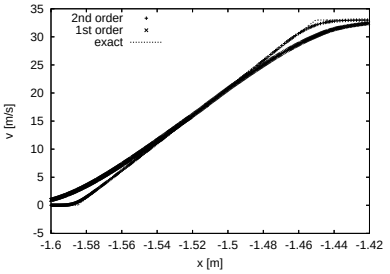

Figure 34: Velocity: Rarefaction

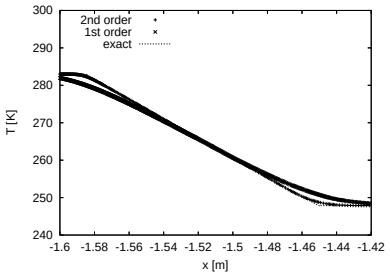

Figure 35: Temperature: Rarefaction

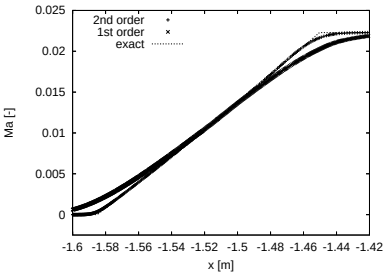

Figure 36: Mach: Rarefaction

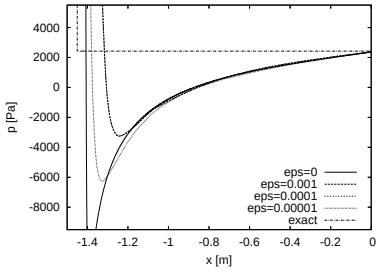

Figure 37: Pressure: 1st order

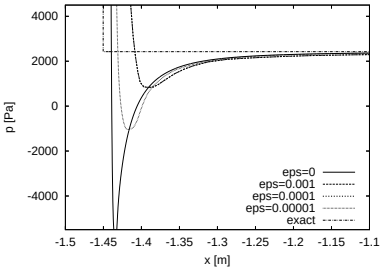

Figure 38: Pressure: 2nd order

6.2 Planar Bubble Collapse

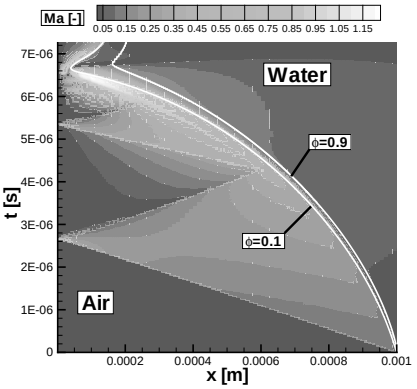

Figure 39: Mach number

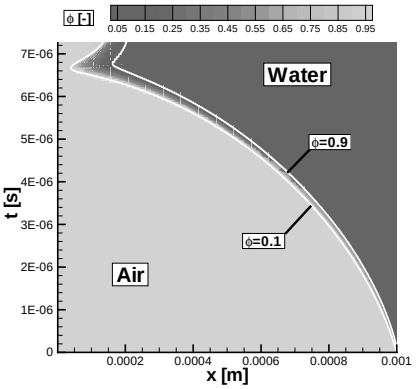

Figure 40: Vapor mass fraction

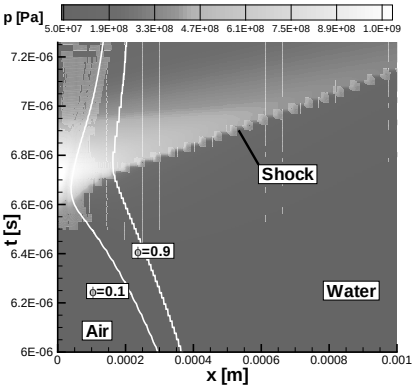

Figure 41: Pressure (zoom)

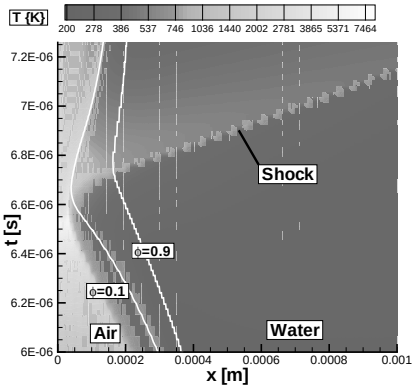

Figure 42: Temperature (zoom)

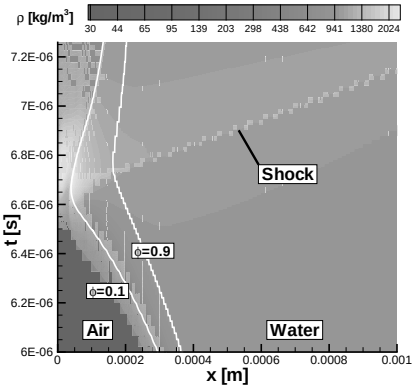

Figure 43: Density (zoom)

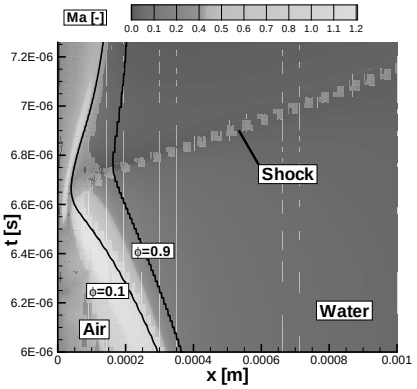

Figure 44: Mach number (zoom)

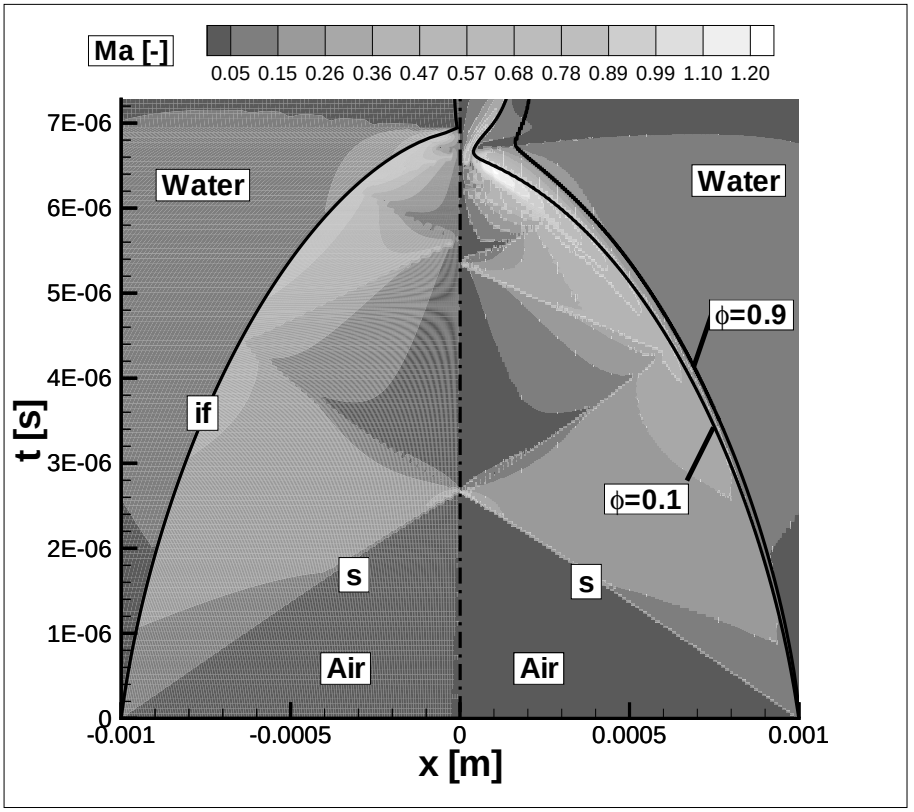

Figure 45: Contour plot of the Mach number (left: BUB, right: 2D code). Dashed line: bubble center, **s**: shock wave, **if**: interface

6.3 Planar Bubble Collapse near to a Rigid Wall

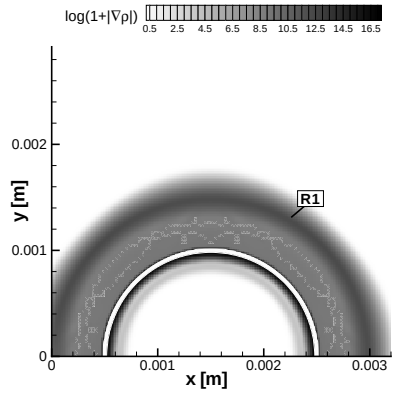

Figure 46: Density gradient magnitude and vapor fraction, $t = 3.20 \times 10^{-7}$ [s]

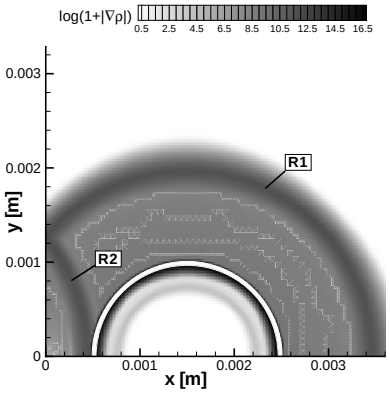

Figure 47: Density gradient magnitude and vapor fraction, $t = 6.30 \times 10^{-7}$ [s]

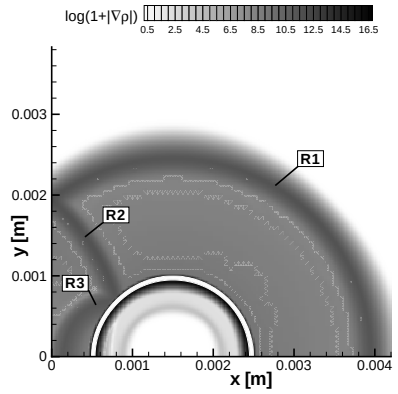

Figure 48: Density gradient magnitude and vapor fraction, $t = 9.50 \times 10^{-7}$ [s]

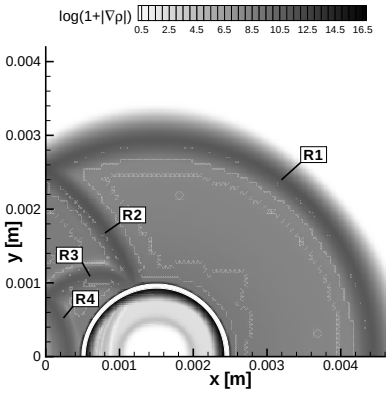

Figure 49: Density gradient magnitude and vapor fraction, $t = 1.26 \times 10^{-6}$ [s]

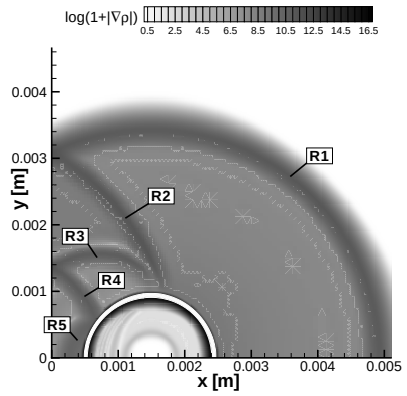

Figure 50: Density gradient magnitude and vapor fraction, $t = 1.58 \times 10^{-6}$ [s]

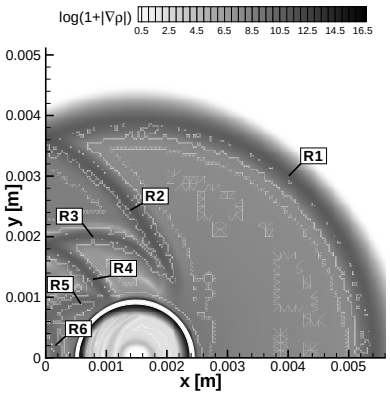

Figure 51: Density gradient magnitude and vapor fraction, $t = 1.90 \times 10^{-6}$ [s]

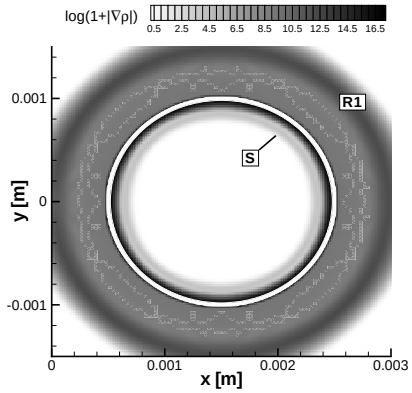

Figure 52: Density gradient magnitude and vapor fraction, $t = 3.20 \times 10^{-7}$ [s]

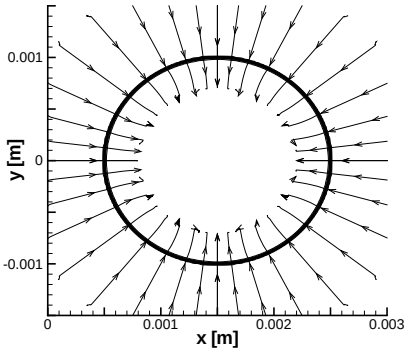

Figure 53: Velocity integral curves and vapor fraction, $t = 3.20 \times 10^{-7}$ [s]

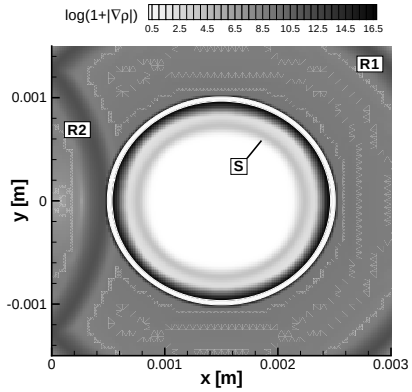

Figure 54: Density gradient magnitude and vapor fraction, $t = 6.30 \times 10^{-7}$ [s]

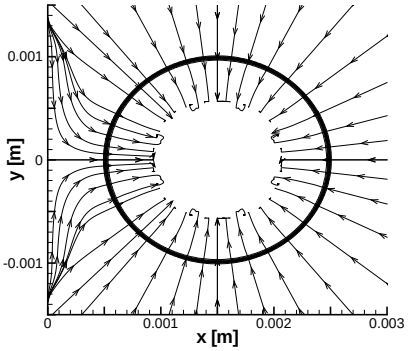

Figure 55: Velocity integral curves and vapor fraction, $t = 6.30 \times 10^{-7}$ [s]

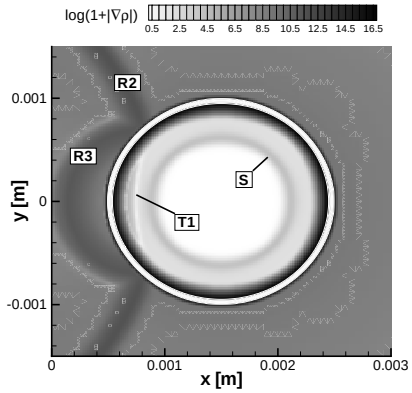

Figure 56: Density gradient magnitude and vapor fraction, $t = 9.50 \times 10^{-7}$ [s]

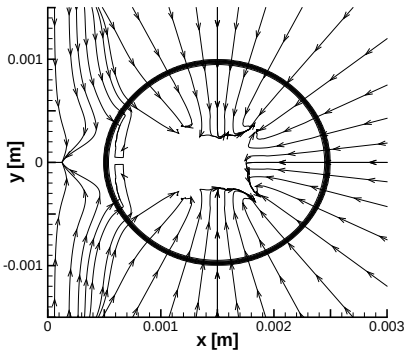

Figure 57: Velocity integral curves and vapor fraction, $t = 9.50 \times 10^{-7}$ [s]

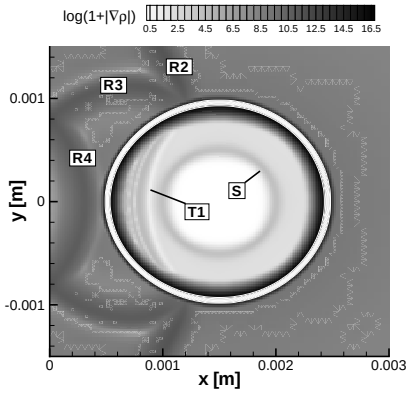

Figure 58: Density gradient magnitude and vapor fraction, $t = 1.26 \times 10^{-6}$ [s]

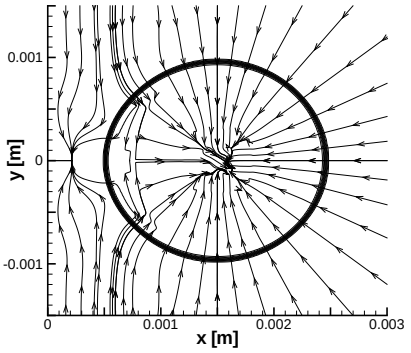

Figure 59: Velocity integral curves and vapor fraction, $t = 1.26 \times 10^{-6}$ [s]

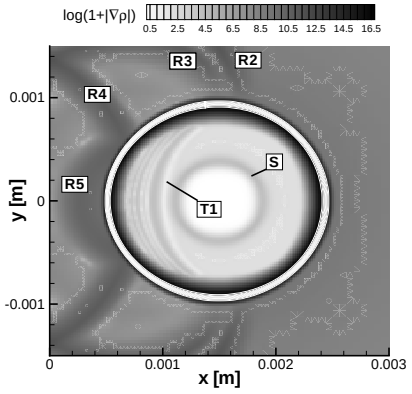

Figure 60: Density gradient magnitude and vapor fraction, $t = 1.58 \times 10^{-6}$ [s]

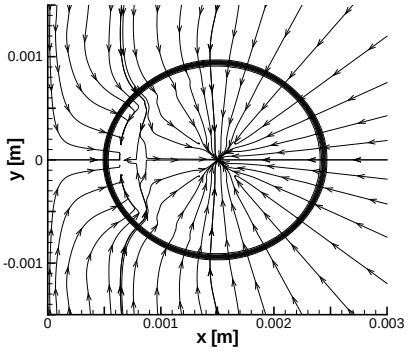

Figure 61: Velocity integral curves and vapor fraction, $t = 1.58 \times 10^{-6}$ [s]

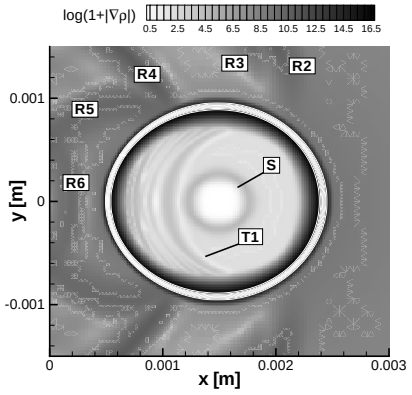

Figure 62: Density gradient magnitude and vapor fraction, $t = 1.90 \times 10^{-6}$ [s]

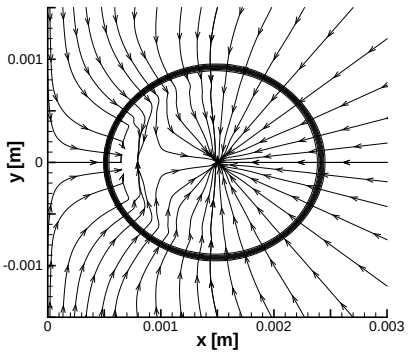

Figure 63: Velocity integral curves and vapor fraction, $t = 1.90 \times 10^{-6}$ [s]

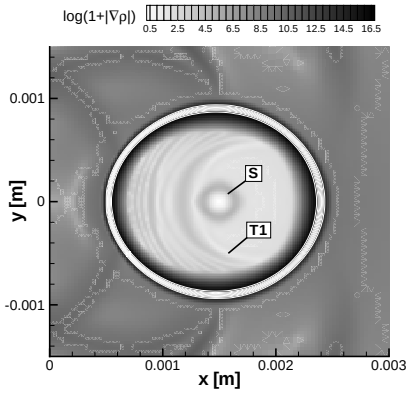

Figure 64: Density gradient magnitude and vapor fraction, $t = 2.21 \times 10^{-6}$ [s]

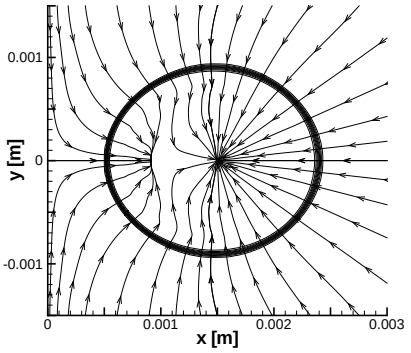

Figure 65: Velocity integral curves and vapor fraction, $t = 2.21 \times 10^{-6}$ [s]

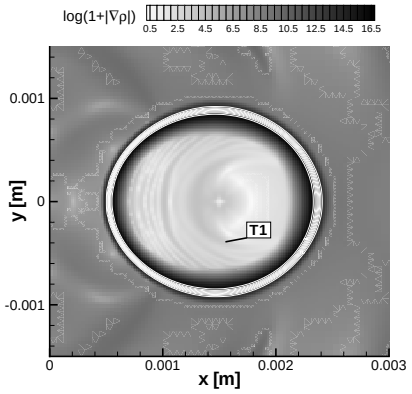

Figure 66: Density gradient magnitude and vapor fraction, $t = 2.53 \times 10^{-6}$ [s]

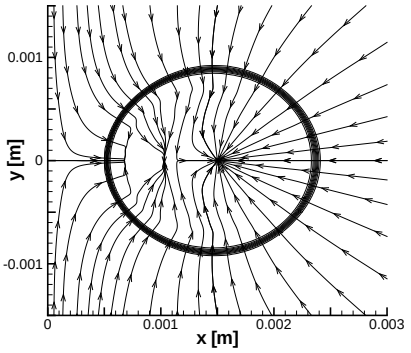

Figure 67: Velocity integral curves and vapor fraction, $t = 2.53 \times 10^{-6}$ [s]

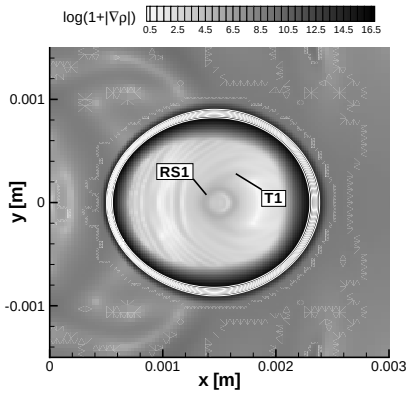

Figure 68: Density gradient magnitude and vapor fraction, $t = 2.84 \times 10^{-6}$ [s]

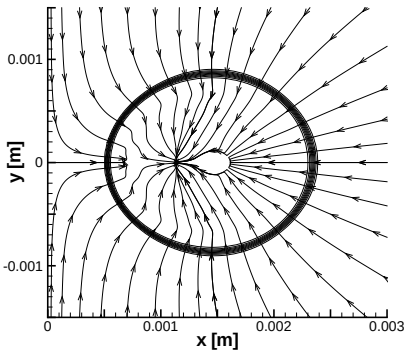

Figure 69: Velocity integral curves and vapor fraction, $t = 2.84 \times 10^{-6}$ [s]

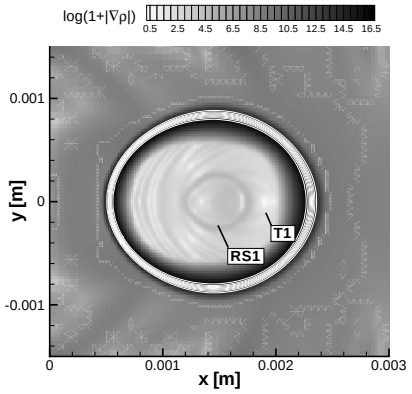

Figure 70: Density gradient magnitude and vapor fraction, $t = 3.16 \times 10^{-6}$ [s]

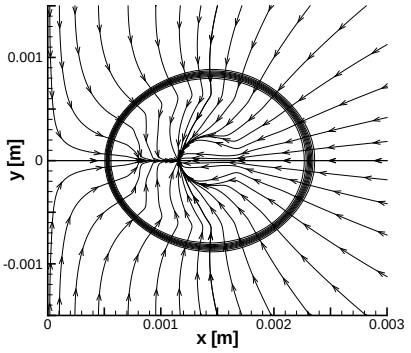

Figure 71: Velocity integral curves and vapor fraction, $t = 3.16 \times 10^{-6}$ [s]

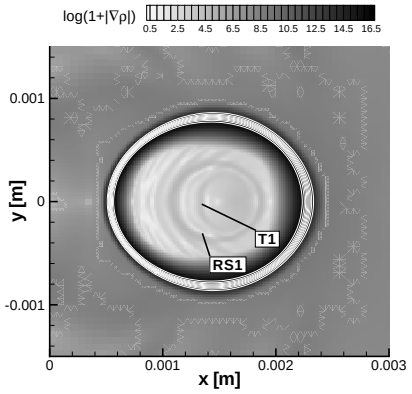

Figure 72: Density gradient magnitude and vapor fraction, $t = 3.48 \times 10^{-6}$ [s]

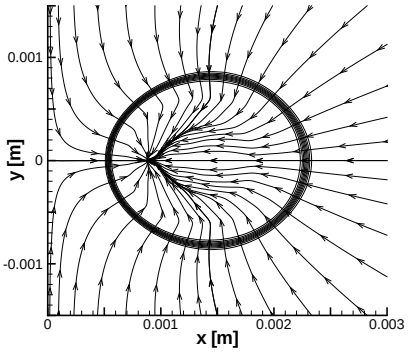

Figure 73: Velocity integral curves and vapor fraction, $t = 3.48 \times 10^{-6}$ [s]

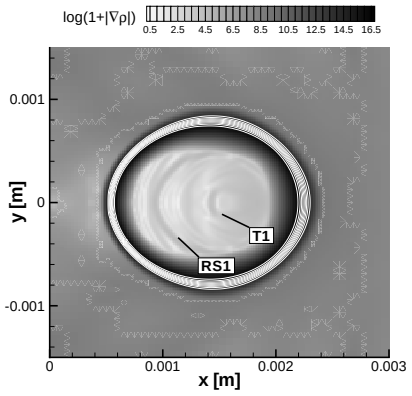

Figure 74: Density gradient magnitude and vapor fraction, $t = 3.79 \times 10^{-6}$ [s]

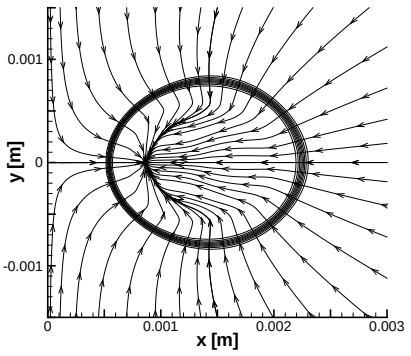

Figure 75: Velocity integral curves and vapor fraction, $t = 3.79 \times 10^{-6}$ [s]

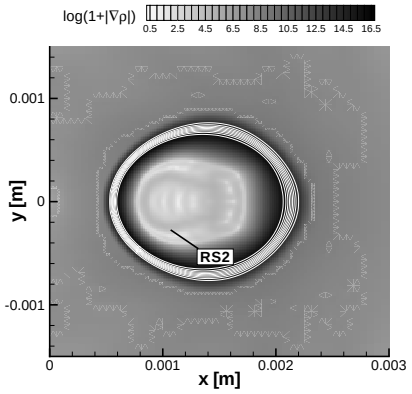

Figure 76: Density gradient magnitude and vapor fraction, $t = 4.74 \times 10^{-6}$ [s]

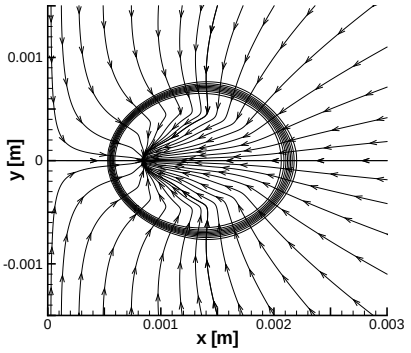

Figure 77: Velocity integral curves and vapor fraction, $t = 4.74 \times 10^{-6}$ [s]

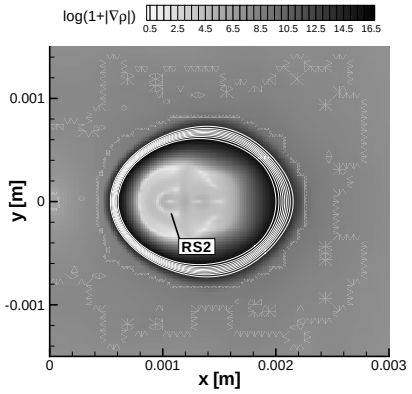

Figure 78: Density gradient magnitude and vapor fraction, $t = 5.14 \times 10^{-6}$ [s]

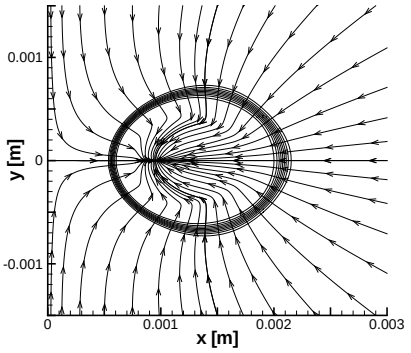

Figure 79: Velocity integral curves and vapor fraction, $t = 5.14 \times 10^{-6}$ [s]

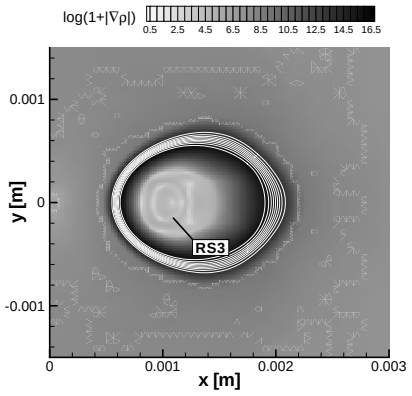

Figure 80: Density gradient magnitude and vapor fraction, $t = 5.65 \times 10^{-6}$ [s]

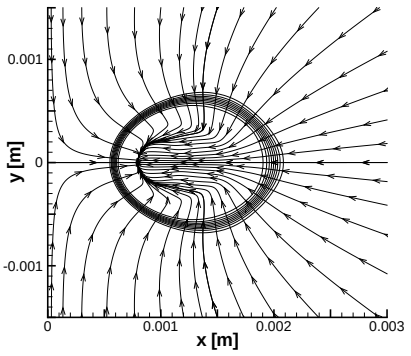

Figure 81: Velocity integral curves and vapor fraction, $t = 5.65 \times 10^{-6}$ [s]

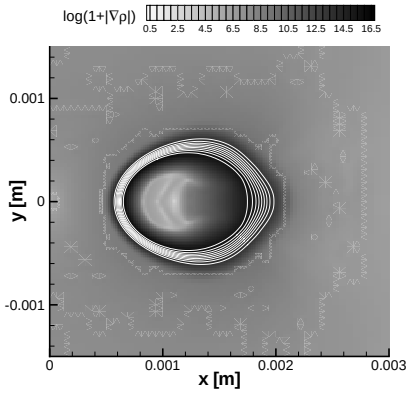

Figure 82: Density gradient magnitude and vapor fraction, $t = 6.32 \times 10^{-6}$ [s]

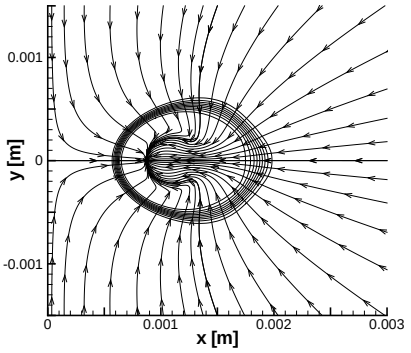

Figure 83: Velocity integral curves and vapor fraction, $t = 6.32 \times 10^{-6}$ [s]

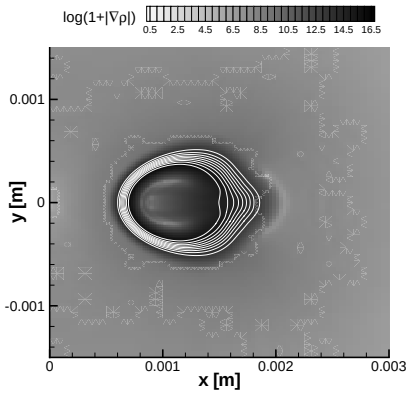

Figure 84: Density gradient magnitude and vapor fraction, $t = 7.11 \times 10^{-6}$ [s]

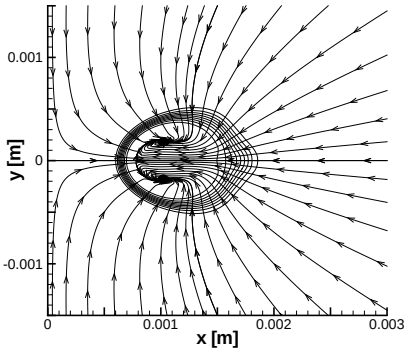

Figure 85: Velocity integral curves and vapor fraction, $t = 7.11 \times 10^{-6}$ [s]

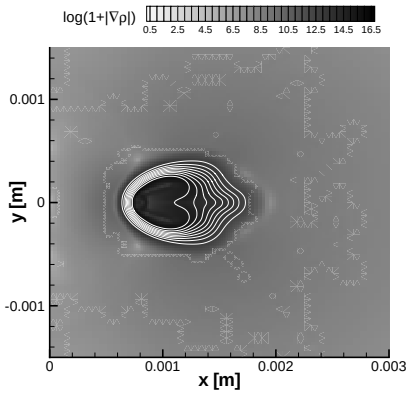

Figure 86: Density gradient magnitude and vapor fraction, $t = 7.89 \times 10^{-6}$ [s]

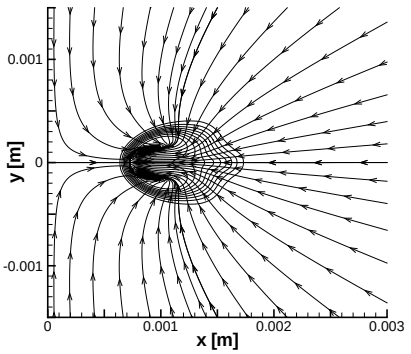

Figure 87: Velocity integral curves and vapor fraction, $t = 7.89 \times 10^{-6}$ [s]

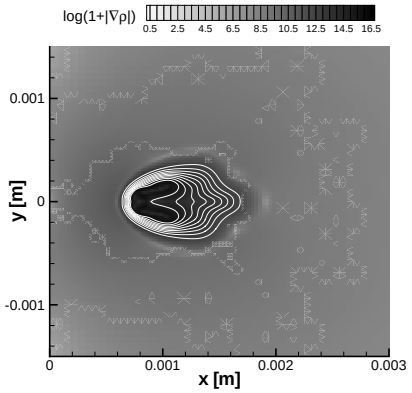

Figure 88: Density gradient magnitude and vapor fraction, $t = 8.20 \times 10^{-6}$ [s]

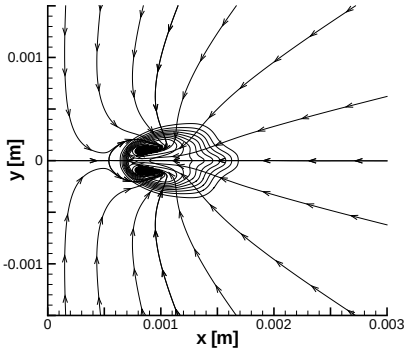

Figure 89: Velocity integral curves and vapor fraction, $t = 8.20 \times 10^{-6}$ [s]

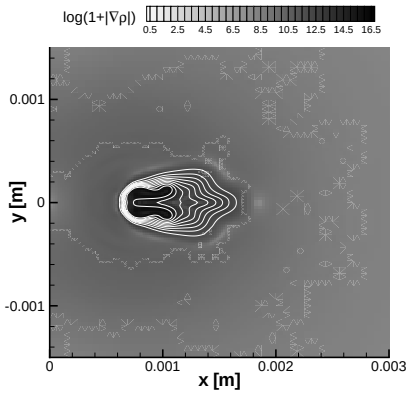

Figure 90: Density gradient magnitude and vapor fraction, $t = 8.50 \times 10^{-6}$ [s]

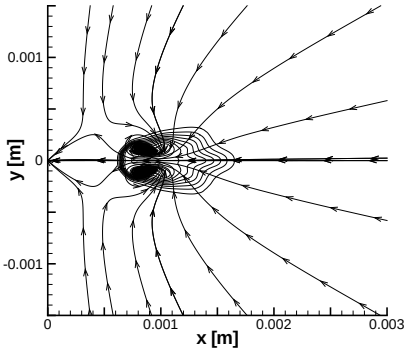

Figure 91: Velocity integral curves and vapor fraction, $t = 8.50 \times 10^{-6}$ [s]

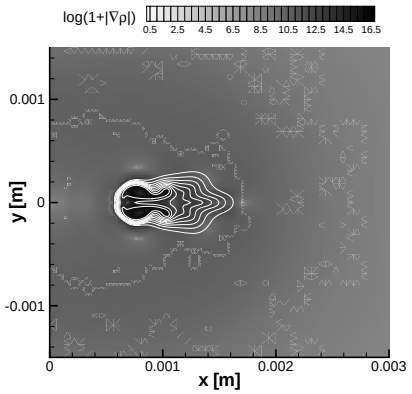

Figure 92: Density gradient magnitude and vapor fraction, $t = 8.78 \times 10^{-6}$ [s]

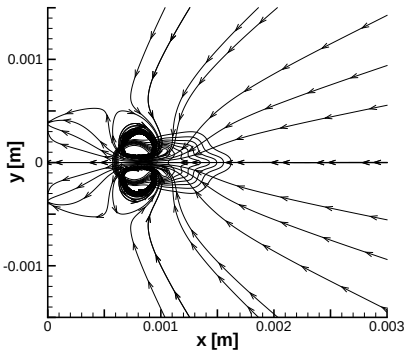

Figure 93: Velocity integral curves and vapor fraction, $t = 8.78 \times 10^{-6}$ [s]

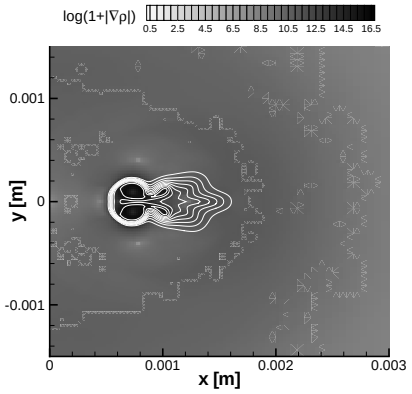

Figure 94: Density gradient magnitude and vapor fraction, $t = 9.04 \times 10^{-6}$ [s]

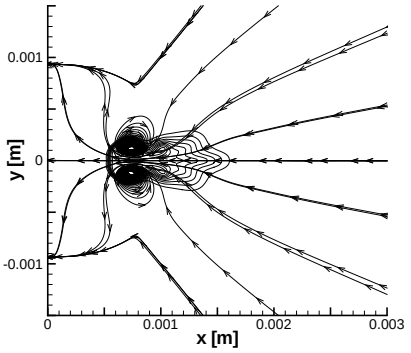

Figure 95: Velocity integral curves and vapor fraction, $t = 9.04 \times 10^{-6}$ [s]

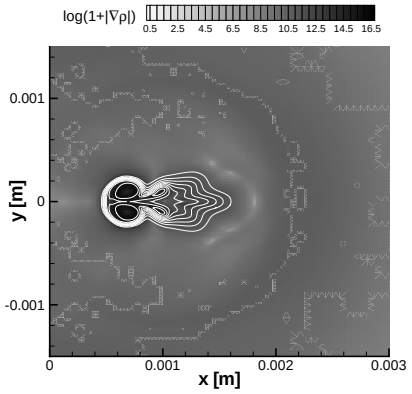

Figure 96: Density gradient magnitude and vapor fraction, $t = 9.30 \times 10^{-6}$ [s]

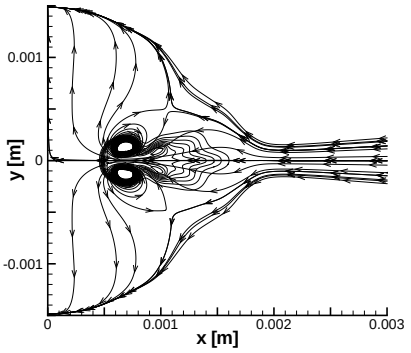

Figure 97: Velocity integral curves and vapor fraction, $t = 9.30 \times 10^{-6}$ [s]

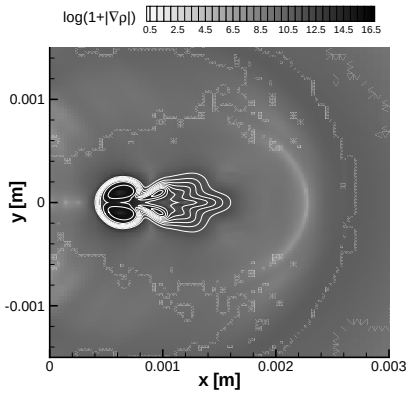

Figure 98: Density gradient magnitude and vapor fraction, $t = 9.56 \times 10^{-6}$ [s]

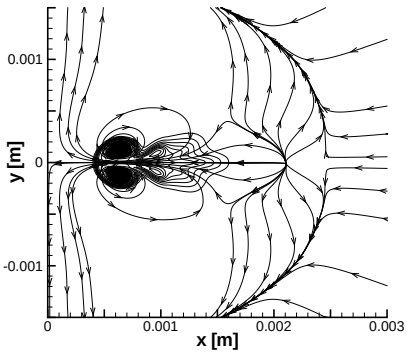

Figure 99: Velocity integral curves and vapor fraction, $t = 9.56 \times 10^{-6}$ [s]

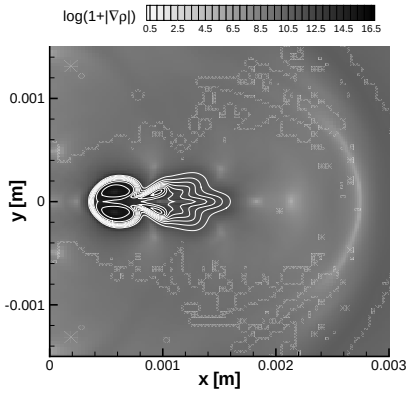

Figure 100: Density gradient magnitude and vapor fraction, $t = 9.82 \times 10^{-6}$ [s]

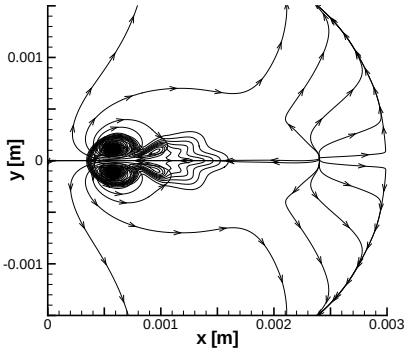

Figure 101: Velocity integral curves and vapor fraction, $t = 9.82 \times 10^{-6}$ [s]

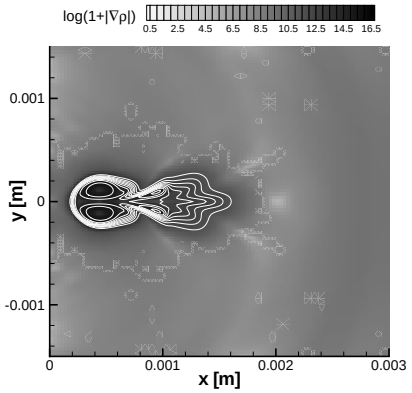

Figure 102: Density gradient magnitude and vapor fraction, $t = 1.07 \times 10^{-5}$ [s]

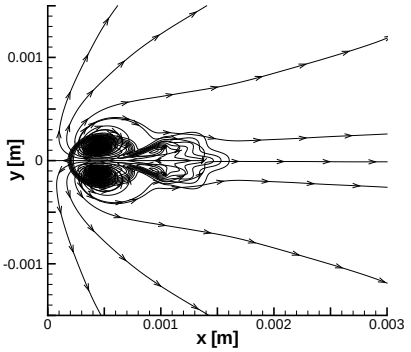

Figure 103: Velocity integral curves and vapor fraction, $t = 1.07 \times 10^{-5}$ [s]

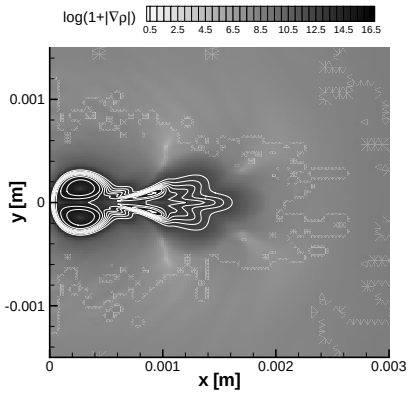

Figure 104: Density gradient magnitude and vapor fraction, $t = 1.21 \times 10^{-5}$ [s]

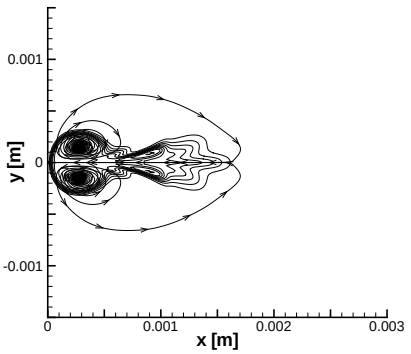

Figure 105: Velocity integral curves and vapor fraction, $t = 1.21 \times 10^{-5}$ [s]

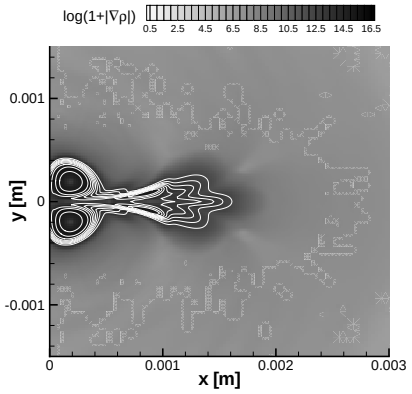

Figure 106: Density gradient magnitude and vapor fraction, $t = 1.35 \times 10^{-5}$ [s]

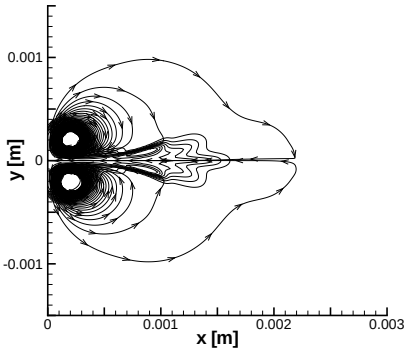

Figure 107: Velocity integral curves and vapor fraction, $t = 1.35 \times 10^{-5}$ [s]

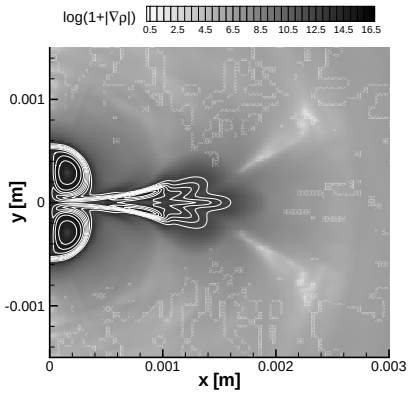

Figure 108: Density gradient magnitude and vapor fraction, $t = 1.50 \times 10^{-5}$ [s]

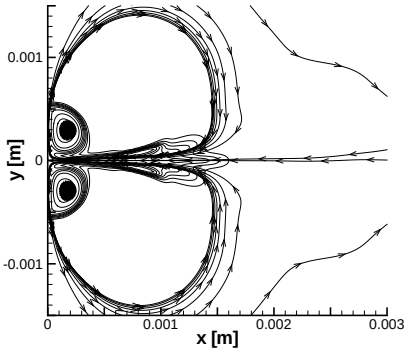

Figure 109: Velocity integral curves and vapor fraction, $t = 1.50 \times 10^{-5}$ [s]

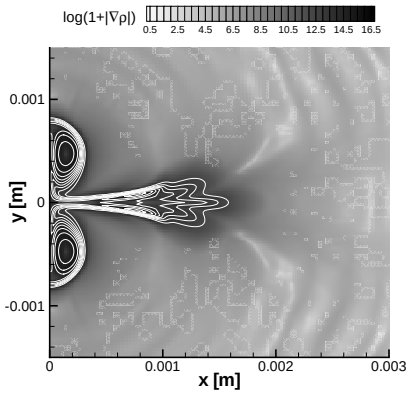

Figure 110: Density gradient magnitude and vapor fraction, $t = 1.73 \times 10^{-5}$ [s]

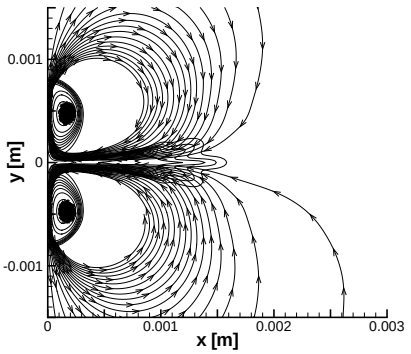

Figure 111: Velocity integral curves and vapor fraction, $t = 1.73 \times 10^{-5}$ [s]

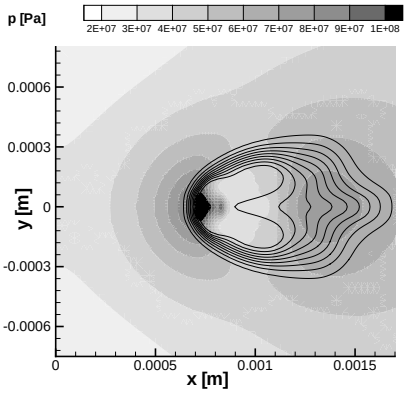

Figure 112: Pressure and vapor fraction, $t = 8.21 \times 10^{-6}$ [s]

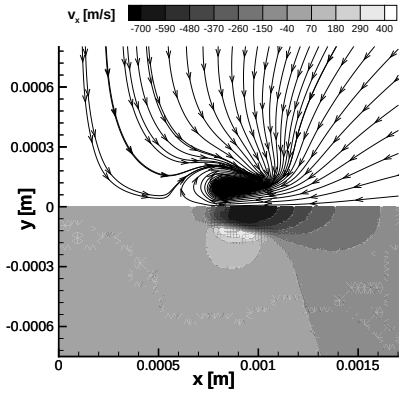

Figure 113: x-velocity and velocity integral curves, $t = 8.21{\times}10^{-6}$ [s]

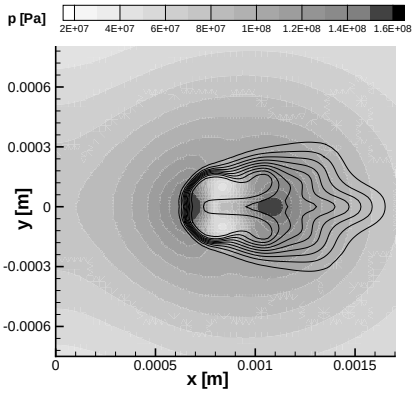

Figure 114: Pressure and vapor fraction, $t = 8.51 \times 10^{-6}$ [s]

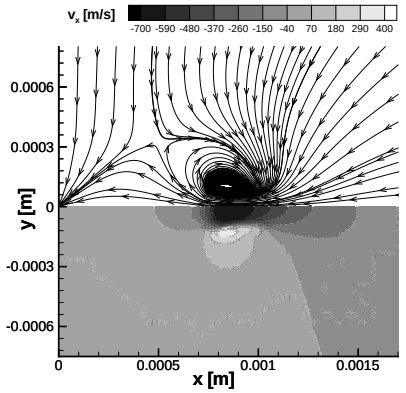

Figure 115: x-velocity and velocity integral curves, $t = 8.51{\times}10^{-6}$ [s]

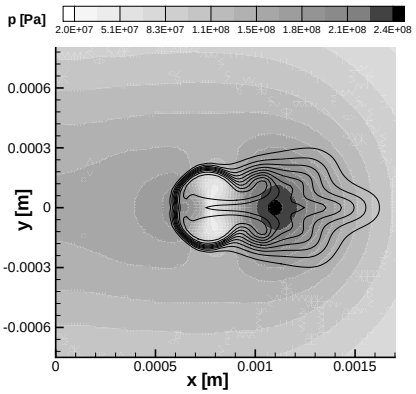

Figure 116: Pressure and vapor fraction, $t = 8.80 \times 10^{-6}$ [s]

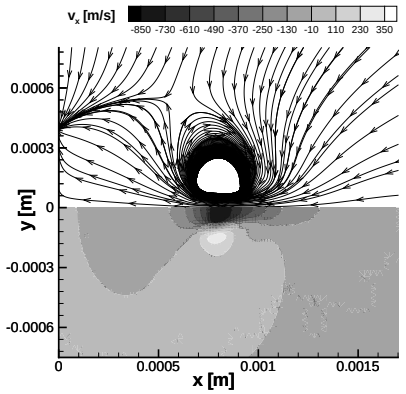

Figure 117: x-velocity and velocity integral curves, $t = 8.80{\times}10^{-6}$ [s]

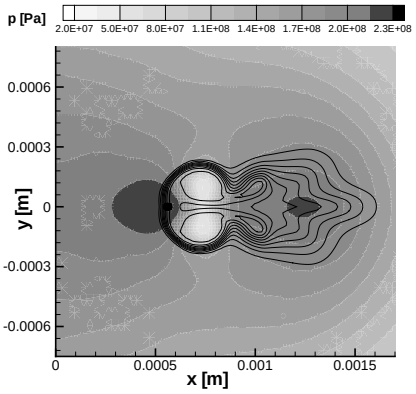

Figure 118: Pressure and vapor fraction, $t = 9.07 \times 10^{-6}$ [s]

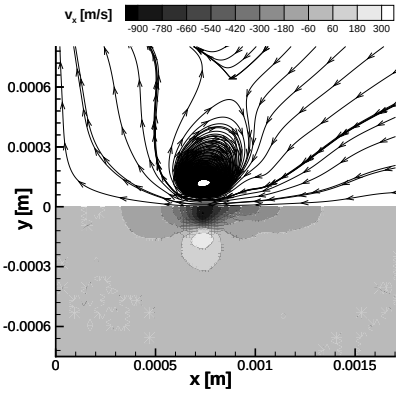

Figure 119: x-velocity and velocity integral curves, $t = 9.07{\times}10^{-6}$ [s]

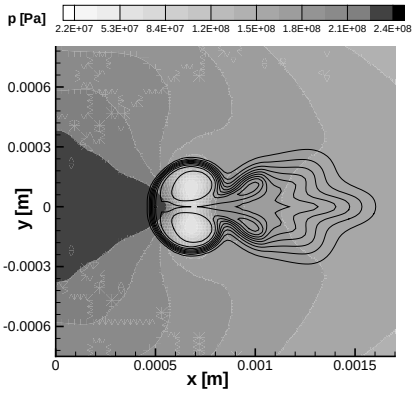

Figure 120: Pressure and vapor fraction, $t = 9.33{\times}10^{-6}$ [s]

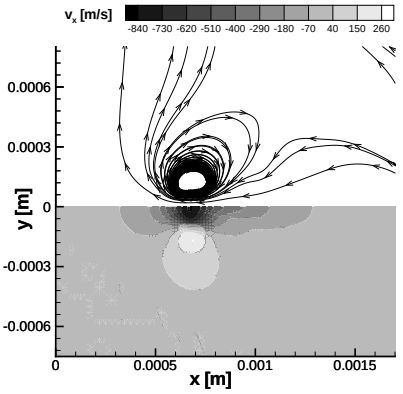

Figure 121: x-velocity and velocity integral curves, $t = 9.33{\times}10^{-6}$ [s]

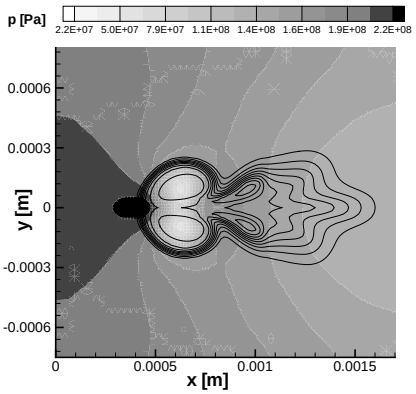

Figure 122: Pressure and vapor fraction, $t = 9.59{\times}10^{-6}$ [s]

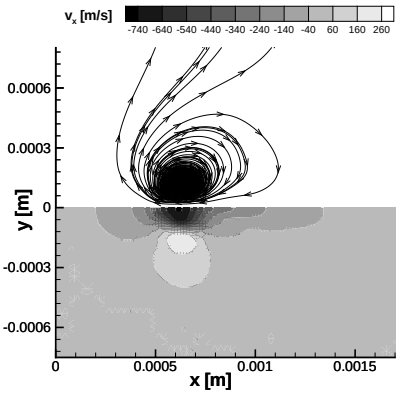

Figure 123: x-velocity and velocity integral curves, $t = 9.59{\times}10^{-6}$ [s]